

# Resonant Trapping in the Galactic Disc and Halo and its Relation with Moving Groups

Moreno, E.<sup>1\*</sup>, Pichardo, B.<sup>1</sup>, Schuster, W. J.<sup>2</sup>,

<sup>1</sup>*Instituto de Astronomía, Universidad Nacional Autónoma de México, Apdo. Postal 70-264, Ciudad Universitaria D.F. 04510, México*

<sup>2</sup>*Instituto de Astronomía, Universidad Nacional Autónoma de México, Apdo. Postal 106, 22800 Ensenada, B.C., México*

4 March 2022

## ABSTRACT

With the use of a detailed Milky Way nonaxisymmetric potential, observationally and dynamically constrained, the effects of the bar and the spiral arms in the Galaxy are studied in the disc and in the stellar halo. Especially the trapping of stars in the disc and Galactic halo by resonances on the Galactic plane, induced by the Galactic bar, has been analysed in detail. To this purpose, a new method is presented to delineate the trapping regions using empirical diagrams of some orbital properties obtained in the Galactic potential. In these diagrams we plot in the *inertial* Galactic frame a characteristic orbital energy versus a characteristic orbital angular momentum, or versus the orbital Jacobi constant in the reference frame of the bar, when this is the only nonaxisymmetric component in the Galactic potential. With these diagrams some trapping regions are obtained in the disc and halo using a sample of disc stars and halo stars in the solar neighbourhood. We compute several families of periodic orbits on the Galactic plane, some associated with this resonant trapping. In particular, we find that the trapping effect of these resonances on the Galactic plane can extend several kpc from this plane, trapping stars in the Galactic halo. The purpose of our analysis is to investigate if the trapping regions contain some known moving groups in our Galaxy. We have applied our method to the Kapteyn group, a moving group in the halo, and we have found that this group appears not to be associated with a particular resonance on the Galactic plane.

**Key words:** Galaxy: disc – Galaxy: kinematics and dynamics – Galaxy: structure – galaxies: spiral structure, bars

## 1 INTRODUCTION

Since the discovery of stellar associations or streams, now also called ‘stellar moving groups’ (Proctor 1869; Eggen & Sandage 1959; Eggen 1977, 1990, 1996a,b; Wilson & Raymond 1938; Roman 1949; Soderblom & Mayor 1993; Majewski 1994; Majewski et al. 1996, and references therein), diverse theories to explain them have emerged, from simple disruptions of open clusters by Galactic tidal effects, to cosmological origins, such as dwarf satellite galaxies or globular clusters (Peñarrubia et al. 2009), to perturbations by resonances with the Galactic bar and/or spiral arms (Dehnen 2000; Fux 2001; Antoja et al. 2009, 2011; Quillen et al. 2011), and also triaxially shaped dark matter haloes (Rojas-Niño et al. 2012). Most likely, all these processes together contribute to form the multiple moving groups

seen today in the Galaxy, but is there one more effective than the others, should we be seeing more groups produced by intrinsic secular processes than the ones produced by disrupted satellites or clusters, or can we identify clearly what phenomenon produces which particular group? Hopefully soon, these and many other questions will be better answered with the impending arrival of the great new large surveys (such as Gaia, SLOAN/APOGEE, the Geneva-Copenhagen Survey, RAVE, SEGUE, etc.) joined to the best theoretical tools to elucidate the different processes.

Meanwhile, one of the intricate problems to solve today is the detection of these groups. Some of the best known methods to identify moving groups in the literature are those using kinematic diagrams, such as the Bottlinger diagram (Bottlinger 1932; Trumpler & Weaver 1953) in the U,V,W space, and Color–Magnitude (CM) diagrams (Eggen 1958, 1959; Eggen & Sandage 1959; Eggen 1960a,b, 1965b, 1970, 1971a,b, 1974, 1976, 1977, 1983, 1990, 1996a,b; Silva et al.

\* E-mail: edmund@astro.unam.mx

2012). Also the method of Lynden-Bell & Lynden-Bell (1995) and of Lynden-Bell (1999) that analyses positions and velocities of globular clusters and satellite galaxies, searching for halo fossil tidal streams that mark orbits followed by satellites merging with the Galaxy. Another method is the one known as Great Circle Cell Counts (GC3) by Johnston et al. (1996), that makes use of the fact that orbits dominated by the spherical outer halo conserve approximately their orbital plane orientation and leave behind ‘great circles’ on the sky. And, methods to search for moving groups in the disc, that work in velocity space, considering that all the stars in a given moving group move toward the same direction (e.g. Hoogerwerf & Aguilar 1999; de Bruijne 1999). A method based on the lumpiness in integrals of motion has been employed by Helmi & de Zeeuw (2000) to study the merger history of our Galaxy. For a review of methods, see this last reference.

Previous work has demonstrated the influence of galactic bars on resonant trapping of orbits on the Galactic plane and out of it. For example particles on bar resonances can exchange or transfer angular momentum to particles in the dark matter halo, driving dynamical evolution ((Lynden-Bell & Kalnajs 1972; Tremaine & Weinberg 1984; Athanassoula 2002; Martínez-Valpuesta et al. 2006; Sellwood 2014; Ceverino & Klypin 2007) and references therein). Although N-body simulations will probably be the best test-bed models to produce studies like the one presented here, it is still intricate to extract information from resonant particles because of their lack of resolution ((Weinberg & Katz 2007a,b)). Therefore, we employ in this work a very detailed Milky-Way steady model that is described in Section 3.

Assuming that a large fraction of moving groups can be explained by intrinsic properties of the Milky Way Galaxy, such as its nonaxisymmetric potential structure, in this work we analyse the trapping of stars by resonances on the Galactic plane produced by these nonaxisymmetric components, and our aim in this and in a second paper is to investigate the possible relation of these trapping regions with some known moving groups in our Galaxy. For this purpose, we have developed a new straightforward tool to analyse the resonant trapping. The method requires the computation of stellar orbits in a nonaxisymmetric Galactic potential, and makes use of diagrams of a ‘characteristic’ orbital energy versus a ‘characteristic’ orbital angular momentum, or versus the orbital Jacobi constant if the Galactic potential employs only the bar in its nonaxisymmetric components.

A sample of halo stars and disc stars in the solar neighbourhood is employed to show how the proposed method works. Our Galactic potential uses mainly the bar as the nonaxisymmetric component, but results are given showing the additional effect of the spiral arms. An axisymmetric potential is also considered, to compare with the main features that arise in the nonaxisymmetric case.

This paper is organised as follows. In Section 2, the observational stellar sample is described. In Section 3, the properties of the three-dimensional Galactic potential employed to compute orbits are summarised. In Section 4 the new method and its technique to analyse resonant trapping is introduced. Section 5 gives a study of periodic orbits on the Galactic plane obtained in a Galactic potential including only the bar in its nonaxisymmetric components; this study

gives the orbital support on which the proposed method is based. Section 6 shows the important influence that resonant families on the Galactic plane can have on stellar orbits at different  $z$ -distances from this plane, which is fundamental for the application of the method to stars in the Galactic halo. In Section 7 this method is complemented by presenting the spectral analysis of the Galactic orbits of the sample stars and of the computed periodic orbits. In Section 8 the method is applied to the Kapteyn moving group in the Galactic halo. Finally, Section 9 presents our conclusions.

## 2 THE OBSERVATIONAL SAMPLE OF STARS

The sample used in this work consists of 1642 halo and disc stars from the catalogues of *uvby- $\beta$*  photometry of high-velocity and metal-poor stars observed at the National Astronomical Observatory, San Pedro Mártir, México (hereafter SPM) (Schuster & Nissen 1988; Schuster et al. 1993, 2006; Silva et al. 2012) with 711, 553, 442, and 143 stars in each of these catalogues, respectively. However, not all of these stars have complete kinematic data, and some of these stars have been repeated in more than one catalogue, which has been amended in the final data base as explained in Silva et al. (2012). Also, about half of the stars in the first catalogue (Schuster & Nissen 1988) have been observed at the Danish telescopes, La Silla, Chile, (hereafter LS): 36.0% of the stars in this first catalogue were observed exclusively in the north at SPM, those with the note ‘N’ in their Table VIII; 50.1% exclusively in the south at LS, those with ‘S’; and 13.8% at both observatories, denoted with ‘N/S’.

The coordinates and proper motions employed in this paper have been taken primarily from: Hipparcos (ESA 1997), Tycho-2 (Høg et al. 2000), and the revised NLTT (Salim & Gould 2003). For a few stars other sources have been used for the proper motions, such as the original NLTT (Luyten 1979a), the LHS (Luyten 1979b), the Lowell Proper Motion Survey (Giclas et al. 1959, 1961, 1975), and the PPM Star Catalogue (Röser & Bastian 1991). In general the proper-motion errors range from 0.5–3.0 mas/yr per component for the best sources, such as Hipparcos and Tycho-2, to as large as  $\gtrsim 10$  mas/yr per component for the other sources. The median errors of the proper motions are  $\pm 1.51$  mas/yr for  $\mu_\alpha$ , and  $\pm 1.20$  mas/yr for  $\mu_\delta$ .

The distances were derived from the photometric absolute-magnitude calibration of Schuster et al. (2004, 2006) and Silva et al. (2012), or from parallaxes in SIMBAD for stars with errors less than 10% or for stars outside the colour range of the photometric calibration. The median error of these distances is  $\pm 6.8$  pc, or  $\pm 9.6\%$  of the distance.

The radial velocities have been selected from the literature, from a number of sources, such as Carney et al. (1994); Barbier-Brossat et al. (1994); Barbier-Brossat & Figon (2000); Ryan & Norris (1991); Fouts & Sandage (1986); Abt & Biggs (1972) and Nordström (private communication). SIMBAD has been consulted to obtain the most precise and up-to-date values possible; about 20% of our radial velocities have been updated from our previous study (Silva et al. 2012). The errors of these radial velocities range from a few tenths of a km s<sup>−1</sup> for the best sources (Carney et al. 1994; Nordström, private communication),

to  $\approx 7 \text{ km s}^{-1}$  for the older sources. The median error of the radial velocities is  $\pm 1.45 \text{ km s}^{-1}$ .

### 3 THE GALACTIC MODEL

In order to construct a comprehensive orbital study of stars in ‘moving groups’ in the Galactic disc and halo, a detailed, observationally restricted, semi-analytic (i.e. with some of the functions numerically solved), three-dimensional model of the Milky Way galaxy, composed of axisymmetric and nonaxisymmetric potentials, is employed (Pichardo et al. 2012). In this model, some modifications are made on the axisymmetric Galactic potential of Allen & Santillán (1991). This axisymmetric potential consists of three components: a disc, a spherical bulge, and a massive spherical halo. The first modifications to build the nonaxisymmetric Galactic potential consist in that all the mass in the spherical bulge is employed to build the Galactic bar, and a small fraction of the total mass of the disc is employed to build the three-dimensional spiral arms. Therefore, only two axisymmetric components are conserved in the final model, the slightly diminished disc and the spherical halo. A boxy bar is employed to represent the Galactic bar; its model is described in Pichardo et al. (2004). The model for the three-dimensional spiral arms, called **PERLAS**, is described in detail in Pichardo et al. (2003). The Galactic potential has been rescaled to the Sun’s galactocentric distance,  $R_0 = 8.3 \text{ kpc}$ , and the local rotation velocity,  $\Theta_0 = 239 \text{ km s}^{-1}$ , given by Brunthaler et al. (2011).

A brief description of the observational/theoretical parameters utilised to restrict the nonaxisymmetric components of the model is presented next and summarised in Table 1 (further details on the parameters of the model and restrictions were introduced in Pichardo et al. (2012)).

#### 3.1 The Galactic Bar

In Pichardo et al. (2004) three different models for the Galactic bar were introduced, which approximate the density model of Freudenreich (1998) of COBE/DIRBE observations of the Galactic centre: a prolate, a triaxial and a triaxial boxy bar. For the computations in this work, we have adopted the triaxial boxy bar model, that fits better the Galactic observations. Table 1 summarises the bar’s structural parameters, such as: the major semi-axis, scale lengths, and axial ratios. The considered total mass for the bar,  $1.6 \times 10^{10} M_\odot$ , is within observational estimations that lie in the range  $1 - 2 \times 10^{10} M_\odot$  (e.g., Kent 1992; Zhao 1994; Dwek et al. 1995; Blum 1995; Stanek et al. 1997; Weiner & Sellwood 1999). The angular speed of the bar and the present orientation of its major axis are still controversial (e.g., Binney et al. 1991; Weiner & Sellwood 1999; Bissantz & Gerhard 2002; Babusiaux & Gilmore 2005; Minchev et al. 2007; Gerhard 2002). We consider  $\phi = 20^\circ$  for the present-day orientation of the major axis of the Galactic bar; this is the angle between this major axis and the Sun-Galactic centre line. A long list of studies have been presented in the literature that estimate the most important dynamical parameter of the Galactic bar, its angular velocity,  $\Omega_B$ , (Gerhard 2011, and references therein). Gerhard (2011) concludes from his review that the

most likely range in  $\Omega_B$  is  $50 - 60 \text{ km s}^{-1} \text{ kpc}^{-1}$ . For our computations, the value  $\Omega_B = 55 \text{ km s}^{-1} \text{ kpc}^{-1}$  is employed, as listed in Table 1. This value is consistent with the recent estimate of  $\Omega_B$  given by Antoja et al. (2014):  $\Omega_B = (1.89 \pm 0.08)\Omega_o$ , with  $\Omega_o$  the local angular velocity; in our potential this gives  $\Omega_B = 54.4 \pm 2.3 \text{ km s}^{-1} \text{ kpc}^{-1}$ .

#### 3.2 The Spiral Arms

The spiral-arm model employed in this work is the one called **PERLAS** (Pichardo et al. 2003); it is formed by a three-dimensional bisymmetric steady potential consisting of a superposition of inhomogeneous oblate spheroids along a logarithmic spiral locus, adjustable to better represent the available observations of the Galactic spiral arms. This simulates the main Galactic spiral arms as in Benjamin et al. (2005) and Churchwell et al. (2009), based on the Spitzer/GLIMPSE database. The position of the spiral arms at the present time is taken as in figure 1 in Pichardo et al. (2012), i.e. the line where these arms emerge at the inner Galactic region lags behind the major axis of the bar making an angle of  $40^\circ$  with this axis. The specific parameters of the spiral arms, such as angular velocity, pitch angle, etc., are provided in Table 1 and more specific details of the parameters are presented in Pichardo et al. (2012). The spiral-arm mass is distributed as an exponential decline along the arms, and their strength is related with their total mass, which is a small fraction of the disc mass. To quantify the strength of the arms, the function  $Q_T$  (Sanders & Tubbs 1980; Combes & Sanders 1981) is computed. The maximum value of  $Q_T$  over the radial extent of the spiral arms, called  $Q_s$ , is a measure of the strength of the spiral arms. In agreement with Buta et al. (2005), and considering that for Sbc galaxies, as for our Galaxy,  $Q_s$  is approximately less than 0.25, the corresponding range in total mass for the spiral arms, calculated from **PERLAS** model, is obtained with  $M_{\text{arms}}/M_{\text{disc}} = 0.04 \pm 0.01$ . We have taken the central value  $3.9 \times 10^9 M_\odot$  for the mass of the spiral arms. Finally, in the same manner as for the Galactic bar, there are different methods to determine the spiral-arm angular velocity; for a review see Gerhard (2011). We use the mean value of  $\Omega_S = 25 \text{ km s}^{-1} \text{ kpc}^{-1}$ , provided by these methods, as listed in Table 1.

### 4 A NEW METHOD TO ANALYSE RESONANT TRAPPING

The orbits of the 1642 stars in the catalogues of Section 2 are computed for different forms of the Galactic potential, such as (1) an axisymmetric case (the rescaled potential of Allen & Santillán (1991)), (2) a nonaxisymmetric case that includes the disc and halo as the axisymmetric components, plus the boxy bar, and (3) the nonaxisymmetric case (2) with the addition of the spiral arms to its nonaxisymmetric components. All the orbits are computed backward in time up to  $10^{10} \text{ yr}$ . Some parameters are obtained in each orbit, such as the orbital energy per unit mass,  $E$ , and the  $z$ -component of angular momentum per unit mass,  $h$  (the  $z$  axis being perpendicular to the Galactic plane); these two important parameters in our method are obtained in all the employed forms of the Galactic potential, and are computed

**Table 1.** Parameters of the Nonaxisymmetric Galactic Components, Sun's Galactocentric Distance and Local Circular Rotation Speed

Parameter	Value	References
<i>Triaxial Boxy Bar</i>		
Major Semi-Axis	3.13 kpc	1
Scale Lengths	1.7, 0.64, 0.44 kpc	1
Axial Ratios	0.64/1.7, 0.44/1.7	
Mass	$1.6 \times 10^{10} M_{\odot}$	
Angle Between Major Axis and the Sun-GC Line	$20^{\circ}$	2
Pattern Speed ( $\Omega_B$ )	$55 \text{ km s}^{-1} \text{ kpc}^{-1}$	3,7
<i>Spiral Arms</i>		
Pitch Angle ( $i$ )	$15.5^{\circ}$	4
Scale Length ( $H_{\star}$ )	3.9 kpc	5
$M_{\text{arms}}/M_{\text{disc}}$	0.04	
Mass	$3.9 \times 10^9 M_{\odot}$	
Pattern Speed ( $\Omega_S$ )	$25 \text{ km s}^{-1} \text{ kpc}^{-1}$	3
$R_0$	8.3 kpc	6
$\Theta_0$	$239 \text{ km s}^{-1}$	6

(1) Freudenreich (1998); (2) Gerhard (2002); (3) Gerhard (2011);  
 (4) Drimmel (2000); (5) Benjamin et al. (2005); (6) Brunthaler et al.  
 (2011); (7) Antoja et al. (2014).

in the Galactic *inertial* frame. Other computed parameters are the Jacobi constant per unit mass,  $J$ , (in the case of the nonaxisymmetric potential including only the boxy bar in its nonaxisymmetric components; case 2 above), the minimum and maximum distances from the Galactic centre, the maximum distance from the Galactic plane, and the orbital eccentricity.

Figure 1 shows results in the axisymmetric potential case. In this potential the Galactic inertial frame is employed to compute the orbits. For the 1642 stars, this figure shows the Lindblad diagram  $E$  versus  $h$ , both constants of motion in the axisymmetric potential. Throughout this work, the units employed for  $h$  are  $10^3 \text{ km s}^{-1} \text{ kpc}$ , and  $10^5 \text{ km}^2 \text{ s}^{-2}$  for  $E$  and  $J$ ; the unit of distance is kpc. As it can be noticed in Figure 1, in the axisymmetric case no structure is visible beyond an approximate homogeneous disc (toward the lower right part of the diagram), and an approximate homogeneous stellar halo (toward the centre-left part of the diagram).

In a nonaxisymmetric potential,  $E$  and  $h$  computed in the Galactic inertial frame are not conserved along the stellar orbit; thus, these are not appropriate parameters to be compared in this case. After several combinations of orbital parameters, it was found that the particular combinations  $(E_{\min} + E_{\max})/2$  versus  $(h_{\min} + h_{\max})/2$  or  $(E_{\min} + E_{\max})/2$  versus  $J$  gave interesting diagrams.  $E_{\min}$ ,  $E_{\max}$  and  $h_{\min}, h_{\max}$  are the corresponding minimum and maximum values of  $E$  and  $h$  along the stellar orbit. We call  $(E_{\min} + E_{\max})/2$  the ‘characteristic’ orbital energy, and  $(h_{\min} + h_{\max})/2$  the ‘characteristic’ orbital angular momentum. In Figure 2 the empirical diagram, characteristic energy versus characteristic angular momentum, is presented, employing a nonaxisymmetric potential that includes the axisymmetric components, plus the central boxy bar (case (2) above). This plot shows a noticeable difference with re-

spect to the axisymmetric case in Figure 1. In this case the observational points gather in several bands that represent the trapping regions produced by different resonances on the Galactic plane, as it will be shown in Section 5. Although our diagrams might seem similar to those of energy versus angular momentum employed by Helmi & de Zeeuw (2000) in their study of moving groups, the results and origin of the formed moving groups are fundamentally different. In the case of Helmi & de Zeeuw (2000), their method was applied to synthetic satellites created from the beginning into an axisymmetric simplified potential of the Galaxy. In this work, on the other hand, we produce a comprehensive study by applying our method in a nonaxisymmetric Galactic potential, where some moving groups might be shaped by resonances generated by the Galactic bar.

In Figure 3, an alternate form to the results in Figure 2 is presented. This figure shows the characteristic orbital energy  $(E_{\min} + E_{\max})/2$  versus the orbital Jacobi constant  $J$ , which is conserved in the reference frame where the bar is at rest. In the same manner as in Figure 2, dots representing stars in the halo and disc agglomerate in noticeable lines or groups, conserving the same structure obtained in that figure. The crowded region of dots to the left in this diagram represents mainly disc stars, while the region to the right contains mainly halo stars.

Figure 4 shows how the diagram in Figure 2 changes when the spiral arms are included in the nonaxisymmetric potential. The difference between both diagrams is negligible for the case of halo stars, i.e., the spiral arms have little effect on halo stars, unlike the bar, where the effect on the formation of groups is clear, most likely due to its much larger mass (approximately ten times the mass of the spiral arms in the Milky Way case), and also because the perigalacticons of these stars approach close or within the bar region. However, the effect of the spiral arms is still of



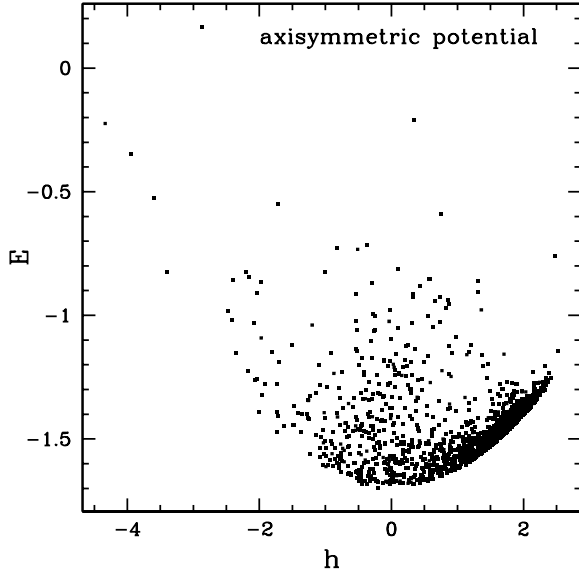


**Figure 1.** The Lindblad diagram of orbital energy per unit mass versus the  $z$ -component of orbital angular momentum per unit mass for the 1642-star sample in the axisymmetric potential model of the Galaxy. The more bound (more negative orbital energies) and largest positive  $z$ -component orbital angular momenta orbits, represented by the darkest region to the lower-right part of the plot, includes mainly Galactic disc stars, while the remainder are mostly halo stars. The units for  $h$  and  $E$  are  $10^3 \text{ km s}^{-1} \text{ kpc}$  and  $10^5 \text{ km}^2 \text{ s}^{-2}$ , respectively.

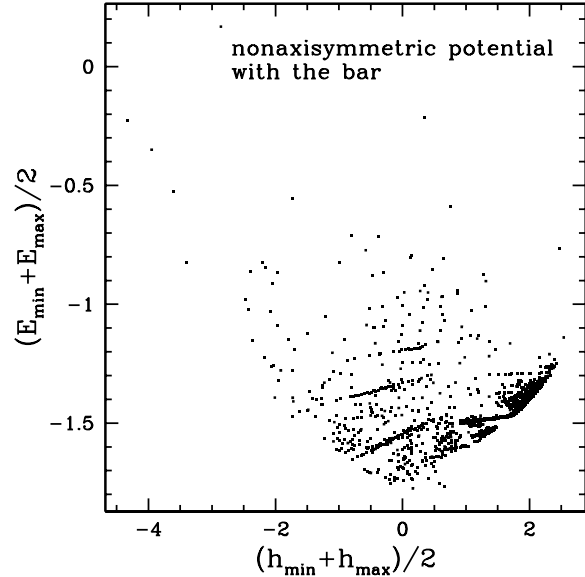
importance on disc stars. In the following, results are given for the Galactic potential including only the bar as a nonaxisymmetric component; in a future study the effects of the spiral arms, in connection with the results presented in the next sections, will be analysed in detail.

Figure 5 is a zoom of Figure 3. In this plot the agglomerations formed in the disc (the left-ward crowded region) and in the halo (the remaining points) are illustrated in more detail. This figure is employed in the next section.

The diagrams as in Figures 2 and 3 are the base of our method to delineate the agglomerations of points in the disc and halo regions. These agglomerations are associated with periodic orbits on the Galactic plane, as it is shown in the next Section 5. The next step is to investigate if known moving groups in the disc and halo are contained in these regions. In the following sections, some additional orbital properties are presented related with these diagrams.

## 5 PERIODIC ORBITS ON THE GALACTIC PLANE

To connect with the diagrams shown in the previous section, several families of periodic orbits *on the Galactic plane* have been computed in the nonaxisymmetric Galactic potential, that includes the axisymmetric components and the central boxy bar. These families of periodic orbits are generated by the presence of the bar, and are defined in the *noninertial* reference frame where the bar is at rest. In this frame, the  $x', y'$  plane is the Galactic plane, with the  $x'$  and  $y'$  axes pointing along the major and minor axes of the bar, respec-



**Figure 2.** Similar to Figure 1, here for the Galactic potential model including only the boxy bar in its nonaxisymmetric components. In this case the diagram plots a ‘characteristic’ orbital energy (in the Galactic inertial frame  $E$  is not conserved along a given orbit) versus a ‘characteristic’ orbital angular momentum ( $h$  is not conserved either), both given by calculating the average of the maximum and minimum values of  $E$  and  $h$  along a given orbit. In this case, noticeable lines of dots (agglomerations of stars in this diagram) are formed in the halo and disc regions, induced by the presence of the bar.

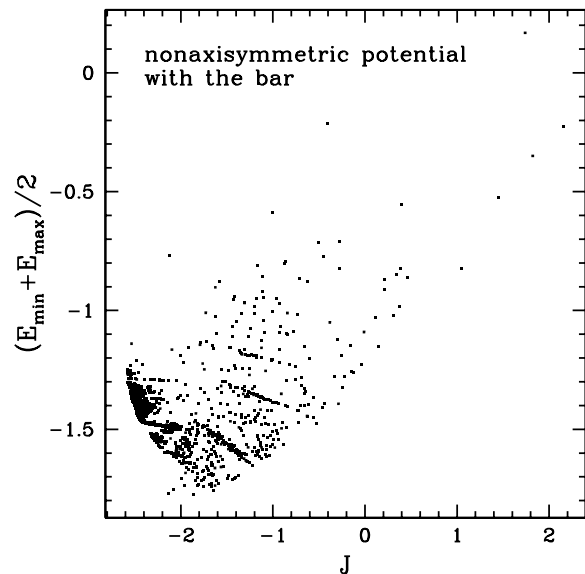


**Figure 3.** An alternate form to present the results in Figure 2; this diagram plots the characteristic orbital energy  $(E_{\min} + E_{\max})/2$  versus the orbital Jacobi constant, in units of  $10^5 \text{ km}^2 \text{ s}^{-2}$ , computed in the reference frame of the bar. As in Figure 2, noticeable agglomerations of stars, induced by the presence of the bar, are formed in the halo and disc regions.

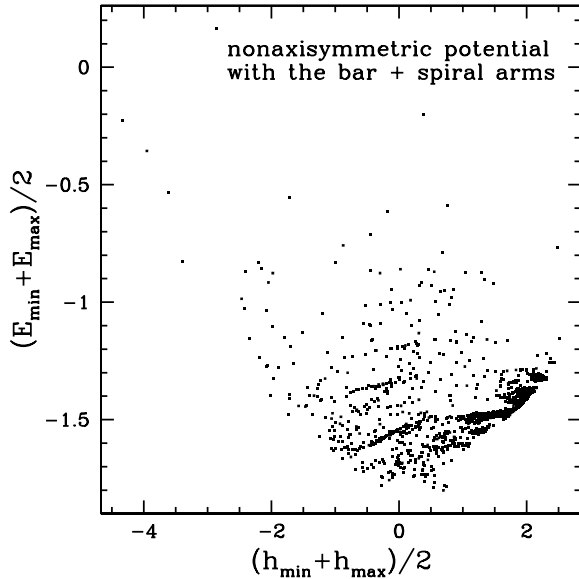


**Figure 4.** As in Figure 2, but now including the spiral arms into the nonaxisymmetric barred potential. Both figures are similar in the case of the halo stars; i.e., the spiral arms have little effect on halo stars, contrary to the case for disc stars shown by the most crowded region to the right of the diagram, where some differences can be noticed.

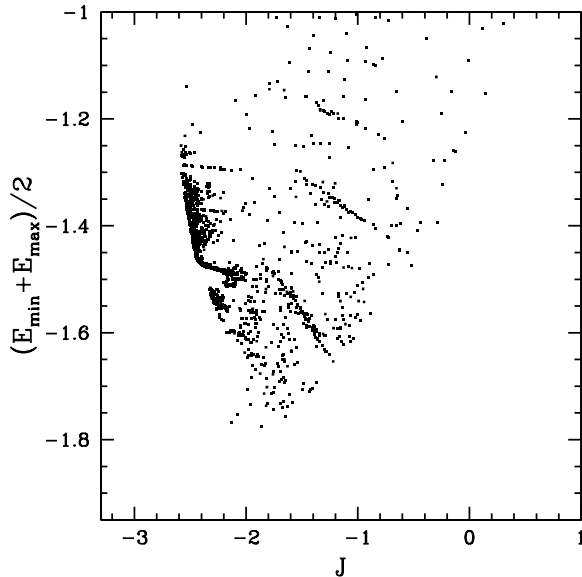


**Figure 5.** This figure shows a zoom of Figure 3 to see in more detail the formation of the agglomerations in the disc and halo regions, and is at the same scale as the following Figure 6, for comparison.

tively; the  $z'$  axis coincides with the  $z$  axis in the inertial reference frame. In this inertial frame the Galactic and bar rotations point in the clockwise direction.

The use of Poincaré-section diagrams has been useful to locate a starting periodic orbit in each family of periodic orbits, from which, using a Newton–Raphson method (Press et al. 1992), we have computed how the orbit evolves

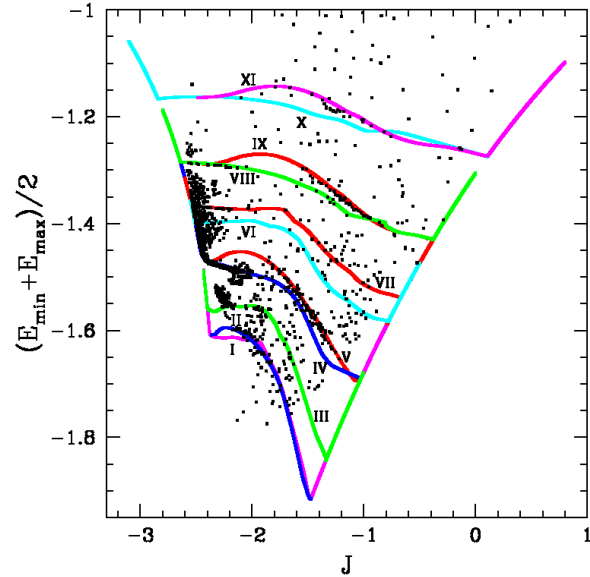


**Figure 6.** Characteristic energy versus  $J$  for the nonaxisymmetric barred Milky Way model, showing in coloured solid lines and with Roman numbers from I to XI, different families of periodic orbits *on the Galactic plane*. These families are defined in the noninertial reference frame where the bar is at rest. The black points are the observational points plotted in Figure 5. Notice that several families coincide with crowded lines of dots in Figure 5.

as the value of the orbital Jacobi constant is varied. For each computed orbit in a given family, the characteristic energy  $(E_{\min} + E_{\max})/2$ , employed in the previous section, and the orbital Jacobi constant  $J$  are obtained; thus, the entire family can be plotted in a diagram as in Figure 3.

In Figure 6 several families of periodic orbits, marked with Roman numbers from I to XI, are plotted in a characteristic energy vs  $J$  diagram, along with the observational points in Figure 5. These families are shown by coloured solid lines. A given colour may represent more than one family. Notice that several of these families of periodic orbits coincide with the crowded lines of dots (groups of stars) induced by the bar (see Figure 5). This occurs even in the halo region of the background observational points, which is surprising, given that the periodic orbits lie on the Galactic plane. This influence of resonances extending with distance from the Galactic plane is analysed in Section 6, for specific families of periodic orbits in Figure 6.

For stellar motion on the Galactic plane analysed in the noninertial reference frame, in Figure 7 we show the Poincaré diagram in the plane  $x', v_{x'}$  for the value of the Jacobi constant  $J = -2.3$  units. Several resonant orbits are shown in this diagram. In Figures 8 and 9 we mark in this Poincaré diagram the families of periodic orbits I to XI considered in Figure 6. Notice that for this particular value of  $J$  the corresponding orbit in a given family can be stable or unstable, i.e. encircled or not by invariant curves.

Figures 10 to 20 show each individual family of periodic orbits given in Figure 6. In these figures the curve of the given family is plotted in two colours, red and green, which show the stable and unstable parts in each curve, respectively. The stability or instability of the computed peri-

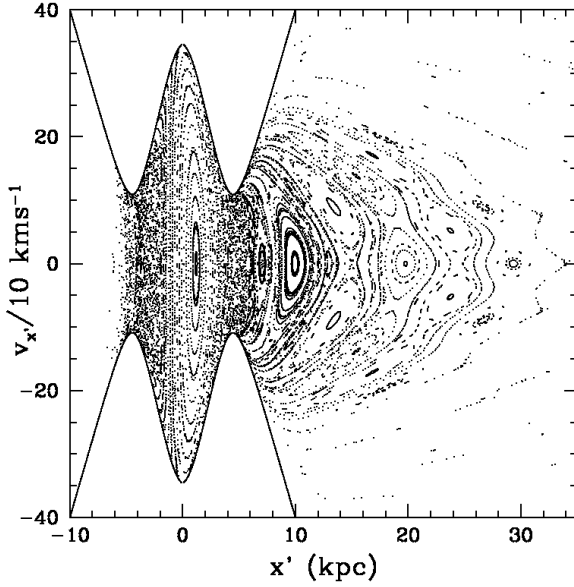


**Figure 7.** For stellar motion on the Galactic plane, this figure shows the Poincaré diagram in the plane  $x', v_{x'}$  for  $J = -2.3$  units.

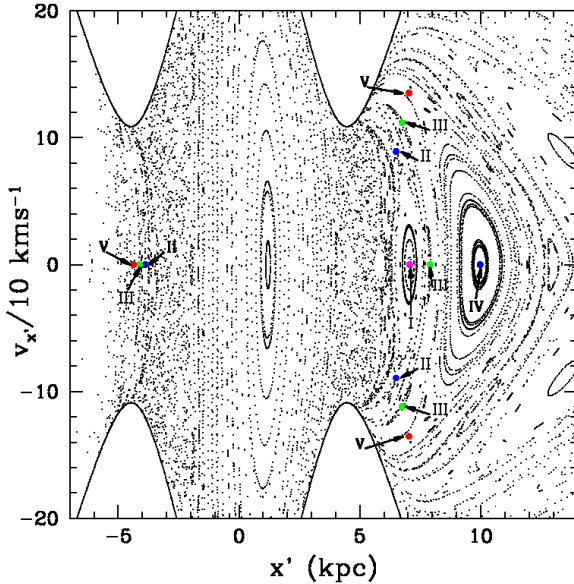


**Figure 8.** This is the left part of Poincaré diagram in Figure 7, showing the positions of families I to V in Figure 6. The colour of points for each family is the same as that employed in Figure 6 for the corresponding curves.

odic orbits in each family was analysed following the method given by Hénon (1965). The agglomerations of points around a given family curve may occur in its stable parts. Also, in these figures five positions are taken in each family curve, labelled from 1 to 5, and their corresponding periodic orbits are shown in the five small frames, including the position number; the scale is the same in these frames, with distances in kpc. These orbits are plotted in the noninertial reference frame where the bar is at rest.

As Figure 6 shows, all the family curves merge on both

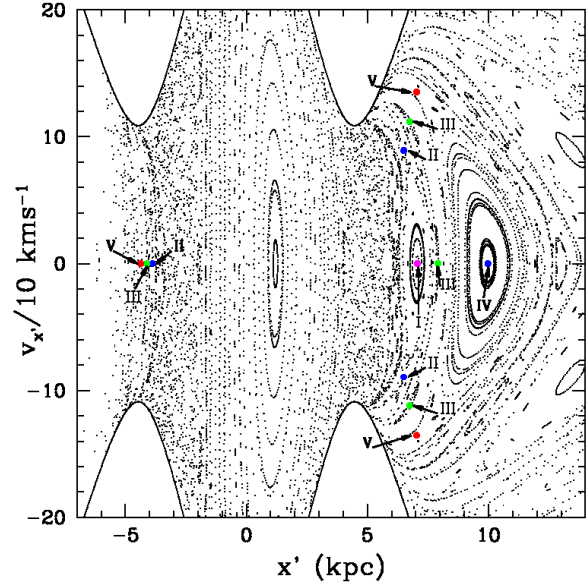


**Figure 9.** Here we show the positions in the Poincaré diagram for families VI to XI in Figure 6. Again, the colour of points corresponds to the colour of curves in Figure 6.

the left and right boundaries of the region where the points distribute. Figures 10 to 20 show that all the details of the periodic orbits tend to disappear at these boundaries, the orbits becoming almost circular. Due to the presence of the bar, this approximation to circular orbits becomes strictly true as the orbital characteristic energy increases.

With respect to the *inertial* Galactic frame, the sense of orbital rotation (of the corresponding orbit in this frame, which in general will not be periodic) in these left and right boundaries in Figure 6 is as follows: in the right boundary, i.e., higher values of  $J$ , the orbital rotation is *retrograde*; in the left boundary, toward the region where the disc component distributes, this rotation is *prograde*. In Figures 10 to 20 a blue starred point on each curve marks the approximate position where the sense of orbital rotation changes in the *inertial* frame, from retrograde to prograde and vice versa. This position corresponds approximately to the periodic orbit in the family that crosses the Galactic centre (nearly localised by one of the five sample periodic orbits in the cases of families I, III, IV, V, VII, VIII, IX; see corresponding figures); this orbit will not have strictly  $h = 0$ , as  $h$  is not conserved.

An additional property of a given family of periodic orbits, is that a point on its curve in a diagram as in Figure 6, i.e., characteristic energy versus  $J$ , is not necessarily associated with a single periodic orbit. If a periodic orbit is not symmetric with respect to one of the axes of the bar, as in families III, VI, VIII, IX, the reflection of the orbit on this axis, which generates a different orbit in the given  $x', y'$  frame, will give the same point in the diagram as the original orbit; i.e., the characteristic energy and  $J$  are the same in both orbits. The existence of the reflected orbit is allowed due to the symmetries of the potential, i.e., the sense of both the  $x', y'$  axes can be changed simultaneously, recovering the original situation. Thus, both types of orbit coexist in the given  $x', y'$  frame.

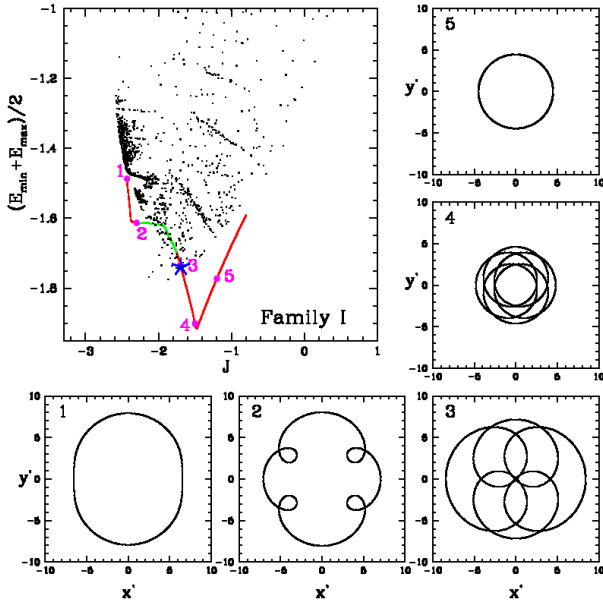


**Figure 10.** This is family ‘I’ in Fig. 6. The stable and unstable parts along the curve are shown with red and green colours, respectively. Five periodic orbits along the family curve are illustrated, numbered from 1 to 5 on the curve and in their frames. The orbits are plotted in the noninertial reference frame where the bar is at rest. The  $x'$  and  $y'$  axes on the Galactic plane point along the major and minor axes of the bar, respectively. The blue star on the family curve shows the approximate position where there is a change in orbital rotation as seen in the *inertial* Galactic frame: from retrograde to prograde going from right to left. In the inertial frame the Galactic and bar rotations point in the clockwise direction. Distances are in kpc.

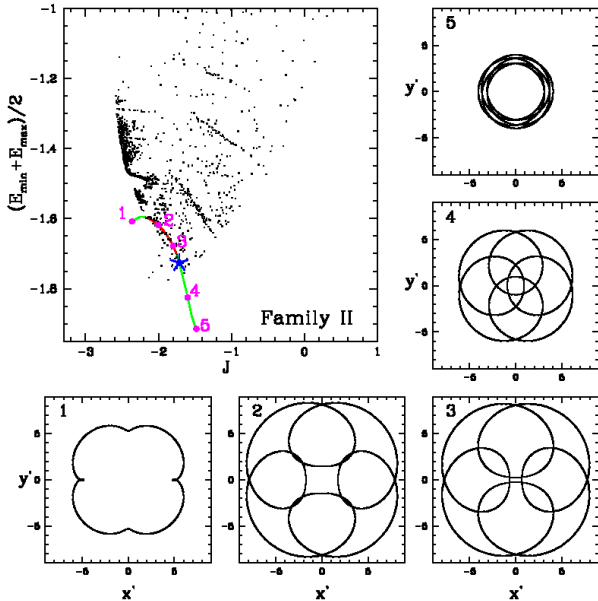


**Figure 11.** The same as Figure 10, here for the family labelled as ‘II’ in Figure 6.

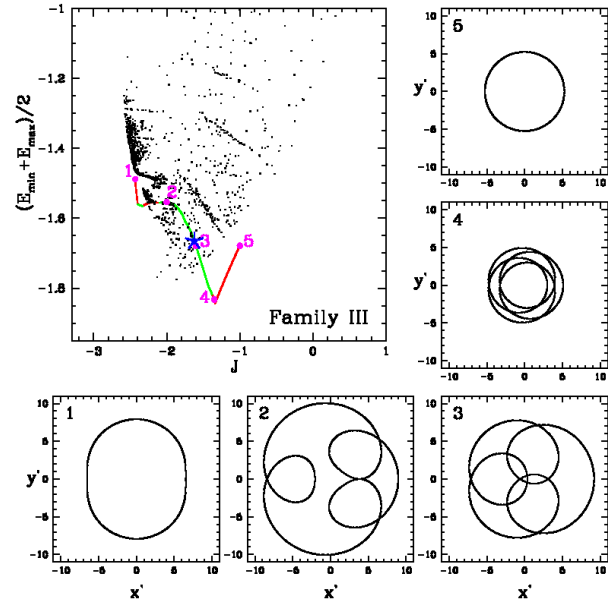


**Figure 12.** The same as Figure 10, here for the family labelled as ‘III’ in Figure 6.

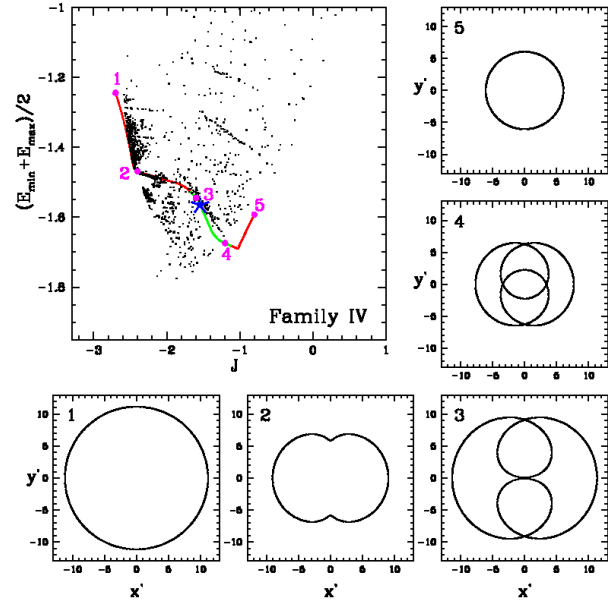


**Figure 13.** The same as Figure 10, here for the family labelled as ‘IV’ in Figure 6.

## 6 INFLUENCE OF RESONANCES ON Z-DISTANCE

In Figure 6 some families of periodic orbits on the Galactic plane coincide with agglomerations of points in Figure 5. These agglomerations occur in the disc and halo regions; thus, the influence of these resonant families does not appear to be restricted necessarily to a region close to the Galactic plane. This influence can extend deep into the halo region.

To show this result, in Figure 21 six agglomerations or regions, A,B,C,D,E,F in different colours, have been considered from the observational points in Figure 5. Regions



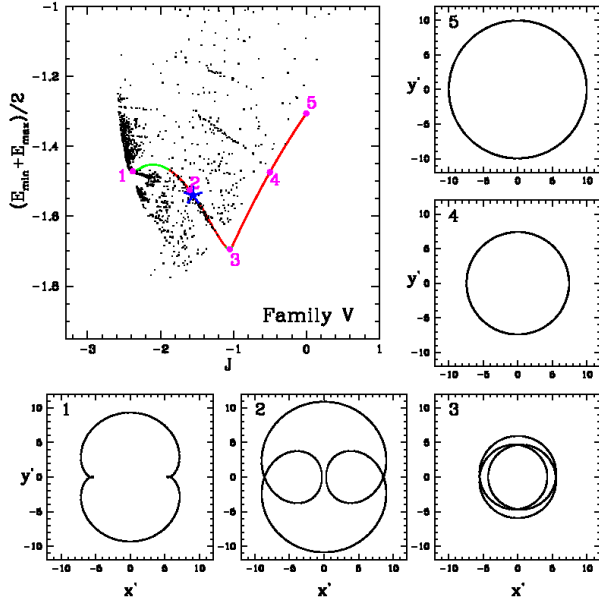


Figure 14. The same as Figure 10, here for the family labelled as ‘V’ in Figure 6.

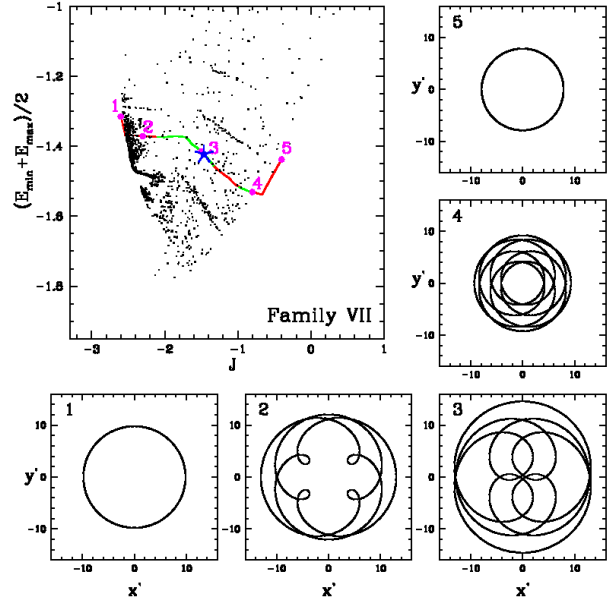


Figure 16. The same as Figure 10, here for the family labelled as ‘VII’ in Figure 6.

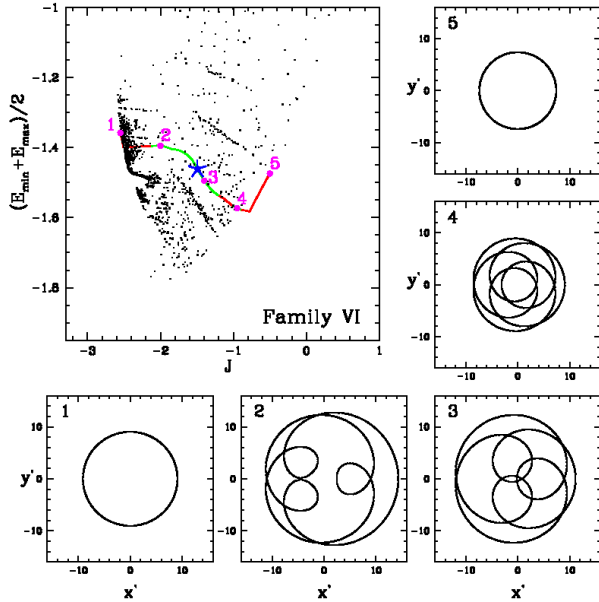


Figure 15. The same as Figure 10, here for the family labelled as ‘VI’ in Figure 6.

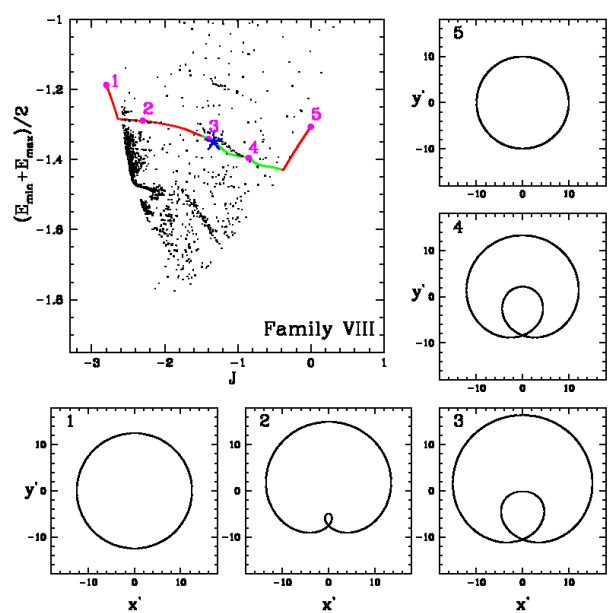


Figure 17. The same as Figure 10, here for the family labelled as ‘VIII’ in Figure 6.

A,B,C are associated respectively with families IV,VII,VIII in Figure 6 (see Figures 13, 16, 17). Regions D,E,F are associated respectively with families V,IX,XI in Figure 6, which have stable parts in these regions (see Figures 14, 18, 20), but probably not with the corresponding neighbouring families IV,VIII,X, which have unstable parts in these regions (see Figures 13, 17, 19).

Figure 22 shows the distribution of the 1642-star sample on the plane of velocities U,V with respect to the inertial Galactic frame, U being negative toward the Galactic centre, and V positive in the direction of Galactic rotation. The points corresponding to stars in the regions A,B,C,D,E,F in

Figure 21 are shown with their colours in that figure, along with a Bottlinger diagram showing some curves of constant orbital eccentricity, obtained with the approximation of an inverse square law for the radial force (Trumpler & Weaver 1953). Regions D,E,F distribute in the prograde-retrograde transition middle zone, with high orbital eccentricities.

For every point (star) in each of the regions A,B,C,D,E,F, the maximum orbital distance from the Galactic plane,  $|z|_{\max}$ , was computed, and corresponding diagrams  $|z|_{\max}$  versus  $J$  were made for each region. These diagrams are shown in Figures 23 to 28. The  $z$ -distance can reach high

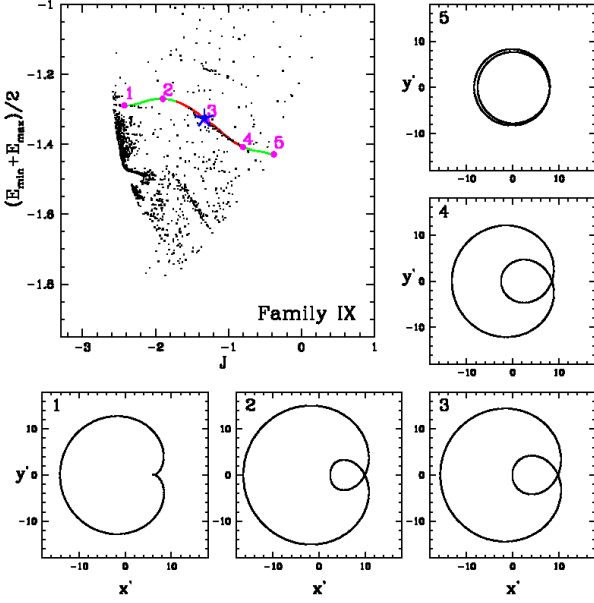


Figure 18. The same as Figure 10, here for the family labelled as ‘IX’ in Figure 6.

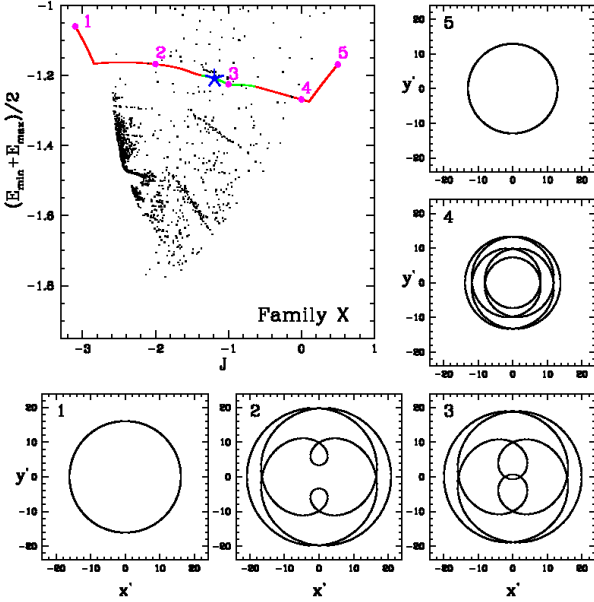


Figure 19. The same as Figure 10, here for the family labelled as ‘X’ in Figure 6.

values, especially in the regions D,E,F for the halo component.

For a sample of stars lying in regions D,E,F and reaching high  $z$ -distances, Figures 29,30,31, respectively, show eight pairs of frames, four of them arranged in the first and second columns and the other four in the third and fourth columns. In each pair, the frame at the left gives the orbital projection on the Galactic plane  $x',y'$  in the reference frame where the bar is at rest, and the corresponding meridional orbit in the plane  $R,z$  is shown in the frame at the right;  $R$  is the distance from the Galactic rotational axis  $z$ . As commented above, stars in these regions D,E,F are mainly

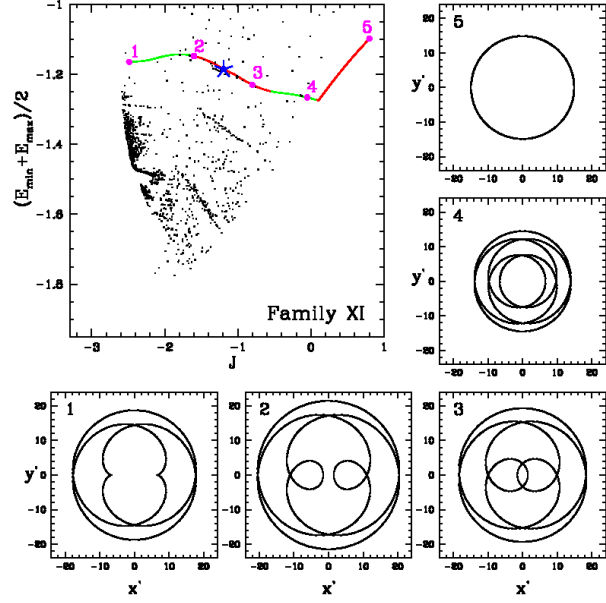


Figure 20. The same as Figure 10, here for the family labelled as ‘XI’ in Figure 6.

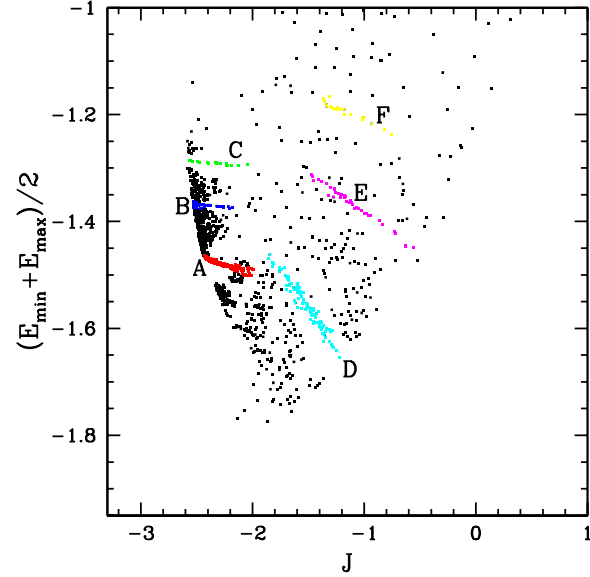
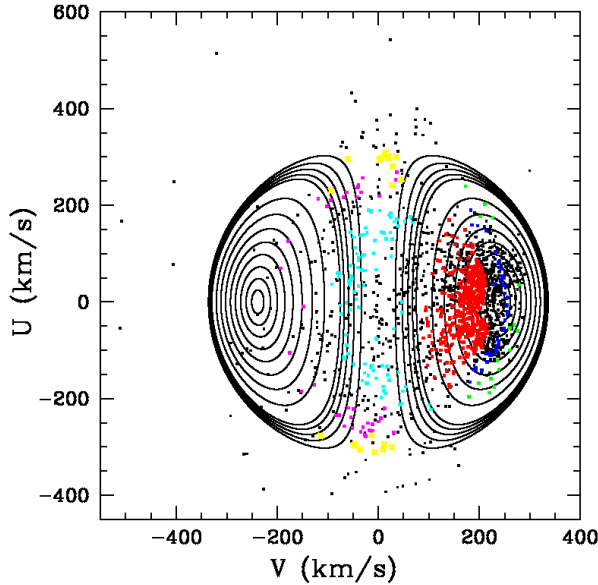


Figure 21. Six regions A,B,C,D,E,F of observational points from Figure 5, shown in different colours. Regions A,B,C are associated respectively with families IV,VII,VIII in Figure 6 (see Figures 13, 16, 17). Regions D,E,F are associated with stable parts of families V,IX,XI in Figure 6, respectively (see Figures 14, 18, 20).

associated with families V,IX,XI, respectively. This can be noticed comparing the orbital projections on the Galactic plane in these figures with the form of the periodic orbits in families V,IX,XI (see Figures 14, 18, 20). Figure 29 shows in the third pair of frames at the left side an orbit which seems to be associated with the family IV, and Figure 31 shows in the second and fourth pairs of frames at the left side two examples of orbits which seem to be associated with the family X, but their projections on the Galactic plane



**Figure 22.** The 1642-star sample in the  $U,V$  velocity plane. These velocities are with respect to the inertial Galactic frame;  $U < 0$  toward the Galactic centre. Regions A,B,C,D,E,F in Figure 21 are shown with their corresponding colours. Some curves with constant orbital eccentricity in a Bottlinger diagram are also shown. From the inner to outer curves in the prograde and retrograde parts, the values of the eccentricity are 0.1,0.2,0.3, ...,0.9,0.92,0.94,0.96,0.98 .

have departed considerably from the unstable periodic orbit in this family X. The conclusion from Figures 29,30,31 is that some resonances *on the Galactic plane* can trap stars reaching high  $z$ -distances from this plane. In their  $N$ -body models of barred galaxies, Ceverino & Klypin (2007) found that particles in the halo with a  $z$ -distance lower than 3 kpc could be trapped by the corotation and inner Lindblad resonances. In our case, for the analysed resonances, the trapping  $z$ -distance can be larger.

As it is shown in Figures 25 to 28, for the regions C,D,E,F there is some internal separation of points for the  $|z|_{\max}$ -distance. This separation is also present when we compute the orbits in the axisymmetric potential obtained by transforming the bar back into the original spherical bulge (see Section 3). Figures 32 to 34 show the situation in the regions D,E,F. In these figures we plot  $|z|_{\max}$  versus  $r_{\max}$ , with  $r_{\max}$  the maximum orbital distance from the Galactic centre. The red points are obtained with the axisymmetric potential and the blue points with the nonaxisymmetric potential.

The separation in  $|z|_{\max}$  in the regions C,D,E,F seems to be associated with an orbital transition between low- and high- $|z|$  orbital domains. In Figure 35 we show how the maximum  $|z|$ -amplitude varies in time for ten member stars in the region F; the present time is at  $t = 0$ . The red curves show the results with the axisymmetric potential and the blue curves the corresponding in the nonaxisymmetric potential. The first three rows in the figure show six orbits with points in the high- $|z|_{\max}$  domain in the axisymmetric potential, but with points in the low- $|z|_{\max}$  domain in the nonaxisymmetric potential. Notice that for the first star in

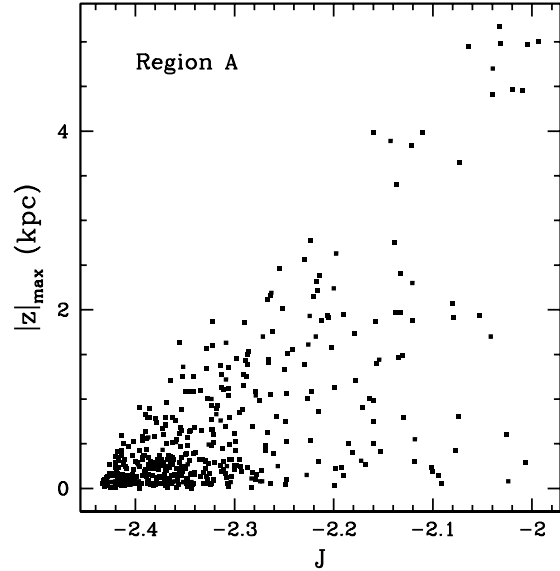


**Figure 23.** Maximum orbital distance from the Galactic plane for the stars in the region A, shown in Figure 21, versus their corresponding  $J$ .

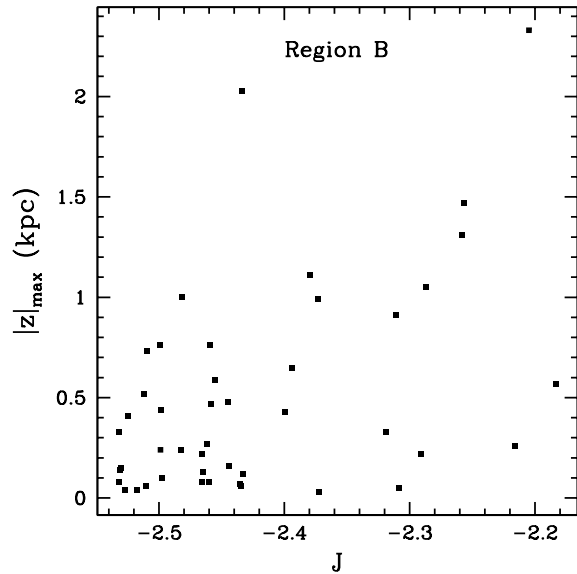


**Figure 24.** Same as in Figure 23, here for the region B of Figure 21.

the second row its orbit has suffered a transition to the low- $|z|_{\max}$  domain, but for the whole computed time of 10 Gyr it has been assigned to the high- $|z|_{\max}$  domain. The last two rows in the figure also show orbital transitions in the axisymmetric and nonaxisymmetric potentials. In particular for stars which can be trapped by the resonance associated to the region F, Figure 35 shows that the presence of the Galactic bar might favor the motion close to the Galactic plane, compared with that obtained in the axisymmetric potential; this result is also present in the resonance associated to the region E, see Figure 33. The separations in  $|z|_{\max}$

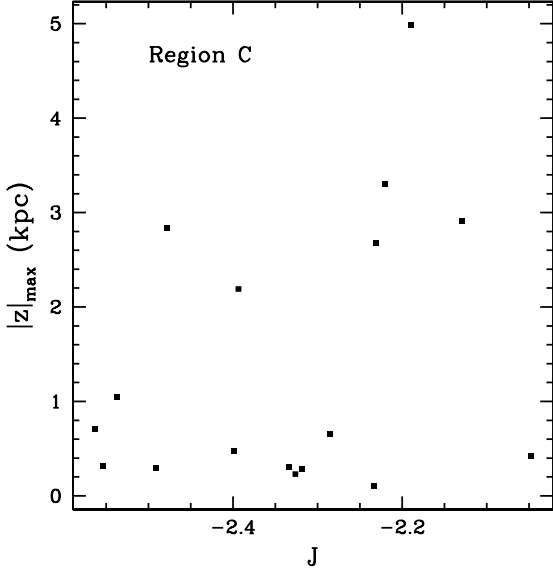


**Figure 25.** Same as in Figure 23, here for the region C of Figure 21.

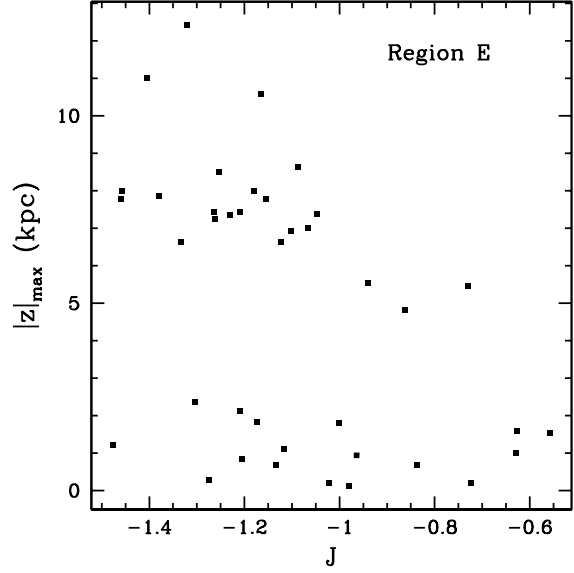


**Figure 27.** Same as in Figure 23, here for the region E of Figure 21.

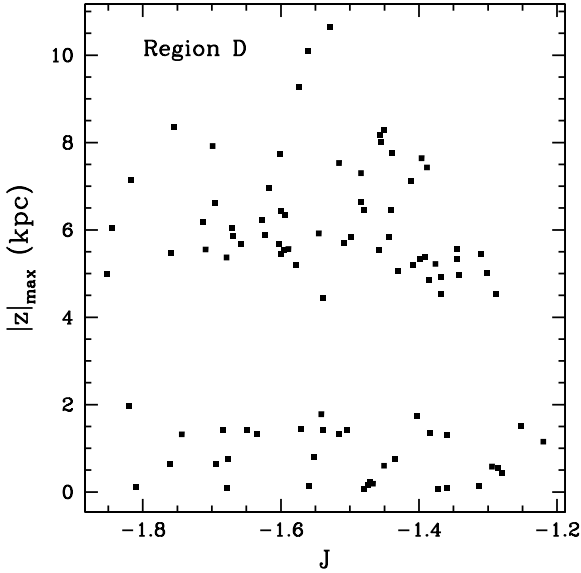


**Figure 26.** Same as in Figure 23, here for the region D of Figure 21.

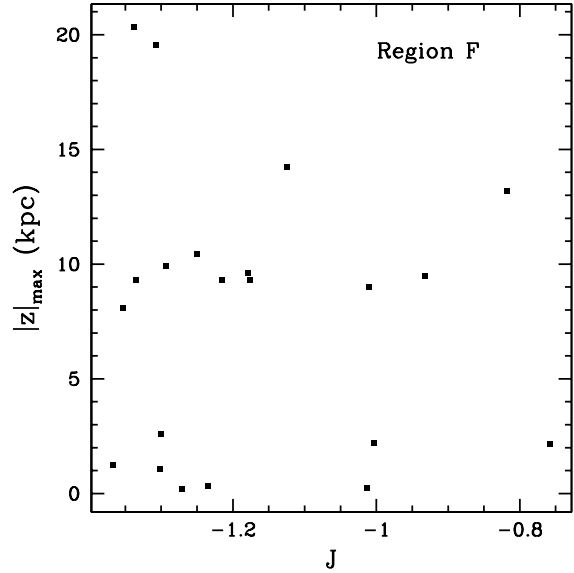


**Figure 28.** Same as in Figure 23, here for the region F of Figure 21.

might be explained by the existence of a major 1:1 resonant family of tube orbits which passes a few kpc above the Sun and which can be appreciated in a number of the ‘vertical’ Poincaré diagrams given in Schuster & Allen (1997), such as figs. 3a, 5a, and 6a. Such a family limits the phase space available for local halo-star orbits, and non-members of these tube orbits must navigate above or below the resonant islands visible in these ‘vertical’ Poincaré diagrams, leading to the separations visible in Figs. 25 to 28 and 32 to 34, and in the behaviour of Fig. 25. Also, stars which belong to such a 1:1 resonant family are not found in the solar neighbourhood, but further above or below the Galactic

plane than the stars of the observational sample described in Section 2, maintaining these empty separations. This issue, and its possible consequences for the external shape of the Galactic halo, needs further study, analysing the resonant families external to the region F to see if they produce a similar behaviour.

This section has shown that resonances on the Galactic plane can have a strong influence on stellar orbits reaching high- $z$  distances from this plane. The stars of the Galactic halo may be strongly affected, acting as test particles influenced by massive nonaxisymmetric structures of the Galactic disc and bar. This effect may have important con-

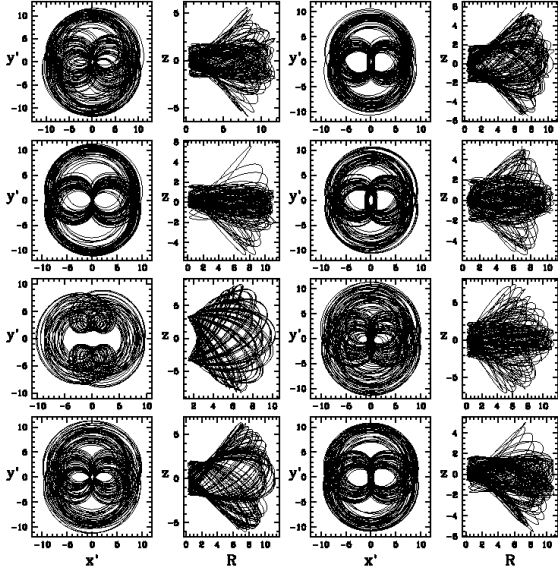


**Figure 29.** For a sample of stars reaching high  $z$ -distances and lying in region D in Figure 21, this figure shows eight pairs of frames, four pairs are arranged in the first and second columns and the other four in the third and fourth columns. In each pair, the frame at the left gives the orbital projection on the Galactic plane  $x', y'$ , in the reference frame where the bar is at rest, and the frame at the right gives the meridional orbit in the plane  $R, z$ .

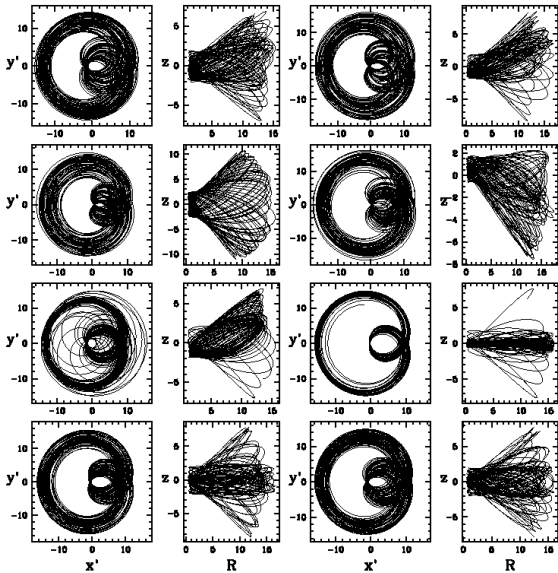


**Figure 30.** As in Figure 29, here for a sample of stars in region E in Figure 21.

sequences in the formation of moving groups in the halo associated with periodic orbits on the Galactic plane.

For stars with high- $z$  distances, there are other factors that may influence their stellar kinematics, such as the triaxiality of the Galactic halo (Peñarrubia et al. 2009; Rojas-Niño et al. 2012, 2015), that with the same resonant process as the nonaxisymmetric bar structures, trigger the

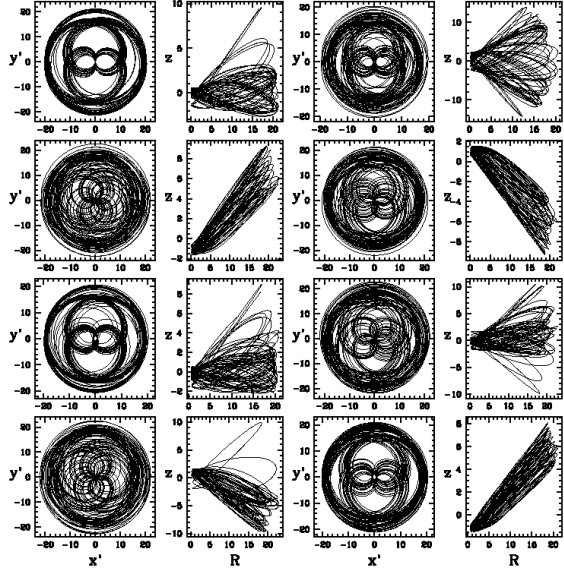


**Figure 31.** As in Figure 29, here for a sample of stars in region F in Figure 21.

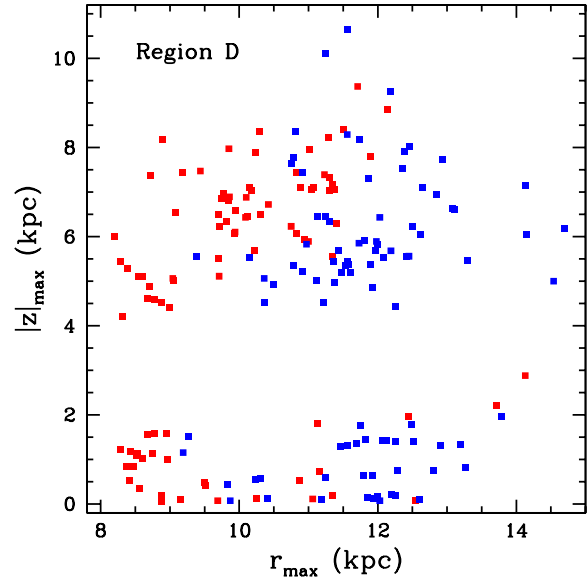


**Figure 32.** For member stars in the region D, this figure shows in the axisymmetric potential (red points) and nonaxisymmetric potential (blue points) the maximum orbital  $z$ -distance versus  $r_{\max}$ , with  $r_{\max}$  the maximum distance from the Galactic centre. The separation in  $|z|_{\max}$  is present in both potentials.

production and support of stellar moving groups. The relative importance of the kinematics imprinted by resonances of the nonaxisymmetric bar structure versus the one imprinted by the triaxiality of the halo is a study that will be presented in a future paper.



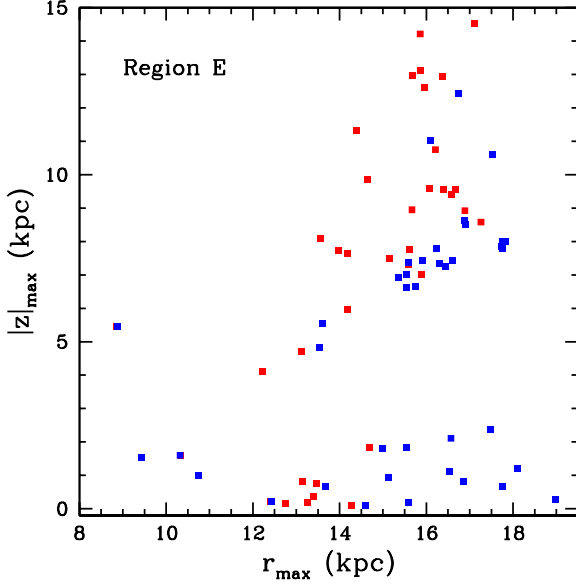


**Figure 33.** As in Figure 32, here for member stars in the region E.

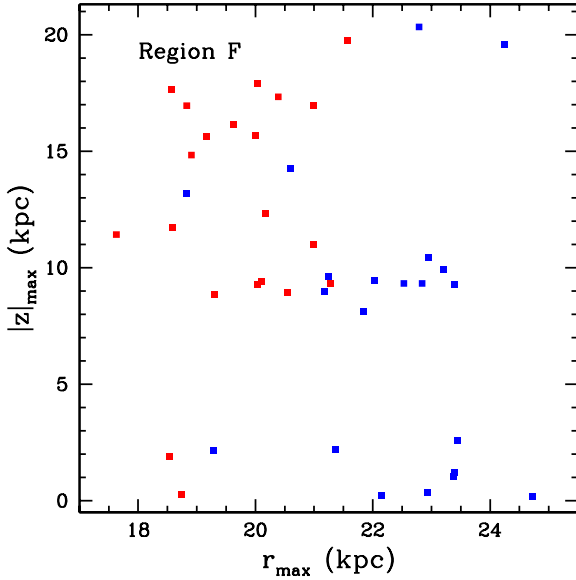


**Figure 34.** As in Figure 32, here for member stars in the region F.

## 7 SPECTRAL ANALYSIS

To complement the analysis presented in previous sections, a spectral analysis of the three-dimensional orbits of the 1642-star sample has been made, and also for the two-dimensional orbits of the several families of periodic orbits on the Galactic plane computed in Section 5. We have considered the method given by Press et al. (1992) for the spectral analysis of unevenly sampled data, and their fast subroutine *fasper* has been employed. In a given orbit, computed in the non-inertial reference frame where the bar is at rest, the spectral analysis was made for each Cartesian coordinate  $x'(t)$ ,  $y'(t)$ ,  $z'(t)$ , or only  $x'(t)$ ,  $y'(t)$  in the case of the families of peri-

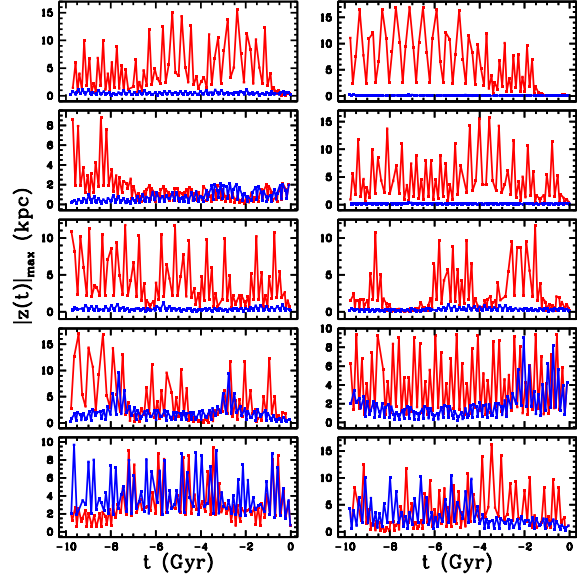


**Figure 35.** Maximum orbital  $|z|$ -amplitude as a function of time for ten member stars in the region F. The red and blue curves show the results in the axisymmetric and nonaxisymmetric potentials, respectively.

odic orbits. The dominant frequency ( $\text{time}^{-1}$ ) was obtained in each coordinate, i.e. the one with the largest amplitude or power in the spectrum.

For the 1642-star sample, Figure 36 compares the ratios of the dominant angular frequencies  $\omega_{x'}$ ,  $\omega_{y'}$ ,  $\omega_{z'}$  (this figure is similar to figure 3.45 in Binney & Tremaine (2008)). The majority of the sample stars distributes around  $\omega_{y'}/\omega_{x'} = 1$ , or with the resonant condition  $\omega \cdot \mathbf{n} = 0$ , with  $\mathbf{n} = (1, -1, 0)$ . Other populated parts appear at the lower region in the figure, especially at the lower left with  $\mathbf{n} = (1, -3, 0)$  and in the diagonal line  $\mathbf{n} = (1, -1, -1)$ . At the right side in this figure there is a concentration around  $\mathbf{n} = (3, -1, 0)$ . The lower region in this diagram corresponds to halo stars, in which  $\omega_{z'}$  decreases (the orbital period in the  $z$ -direction increases).

To make a diagram similar to those constructed in Section 4, in Figure 37 we plot for the 1642-star sample the ratio  $\omega_{y'}/\omega_{x'}$  versus the corresponding orbital Jacobi constant  $J$  (taking  $J \leq 1$  as in Figure 5). Again, several agglomerations of points are obtained, with particular details in the interval  $\approx (-2, -0.5)$  in  $J$ , where regions D,E,F in Figure 21 are located.

The next step is to plot in a diagram like the one shown in Figure 37, the several families of periodic orbits computed in Section 5. Figures 38 and 39 show this diagram separately for each family; the black points in each frame correspond to the sample stars and the coloured lines to the given family. The number of the family is given in each frame and the employed colour is the same as in Figure 6. Notice that the ratio  $\omega_{y'}/\omega_{x'}$  changes in a given family as  $J$  is varied (when there is a transition between two levels in this ratio, its value may oscillate between the two levels and this appears as an overlapping of levels at the transition). The agglomerations of sample stars, which have three-dimensional orbits, are nearly covered by the families of periodic orbits, which lie *on the Galactic plane*.

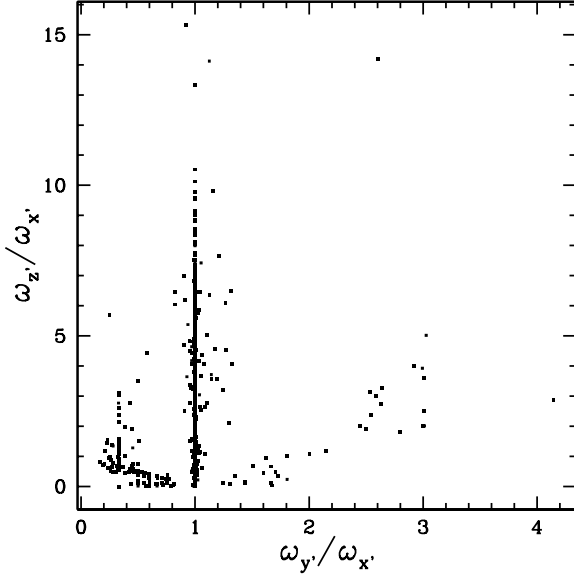


**Figure 36.** Ratios of the dominant orbital angular frequencies in the three Cartesian coordinates  $x'(t), y'(t), z'(t)$  for the 1642 sample stars.

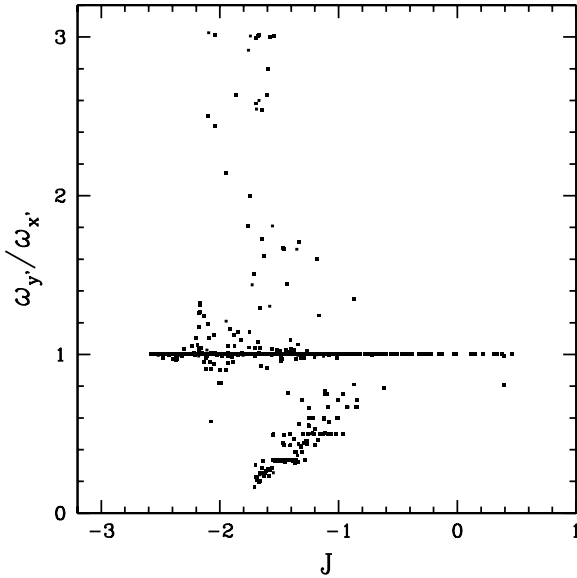


**Figure 37.** The ratio  $\omega_{y'}/\omega_{x'}$  as a function of  $J$  for the 1642-star sample. Here we take  $J \leq 1$  as in the zoom shown in Figure 5.

Now, in particular, the halo regions D,E,F shown in Figure 21 are considered. We have seen that these regions are likely associated with families V, IX, XI, respectively, which have stable parts in the positions of these regions. Thus, it is of interest to see what is the relation region-family: D-V, E-IX, and F-XI in a diagram  $\omega_{y'}/\omega_{x'}$  versus  $J$ . Figures 40, 41, and 42 show the results. The black lines correspond to the family and the red points to the region. These figures show that there are approximate relations between the corresponding region and family. A three-dimensional orbit which may be trapped by a resonant family on the

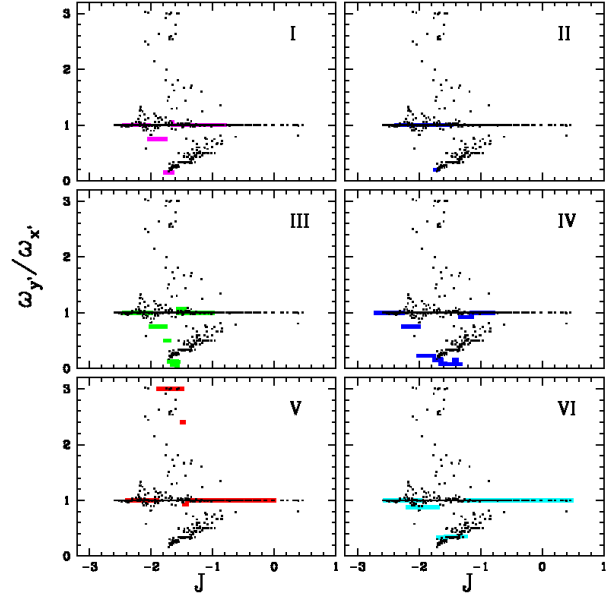


**Figure 38.** The ratio  $\omega_{y'}/\omega_{x'}$  as a function of  $J$  for families of periodic orbits I to VI. The colour of lines in each family is that employed in Figure 6. The black points correspond to the 1642-star sample.

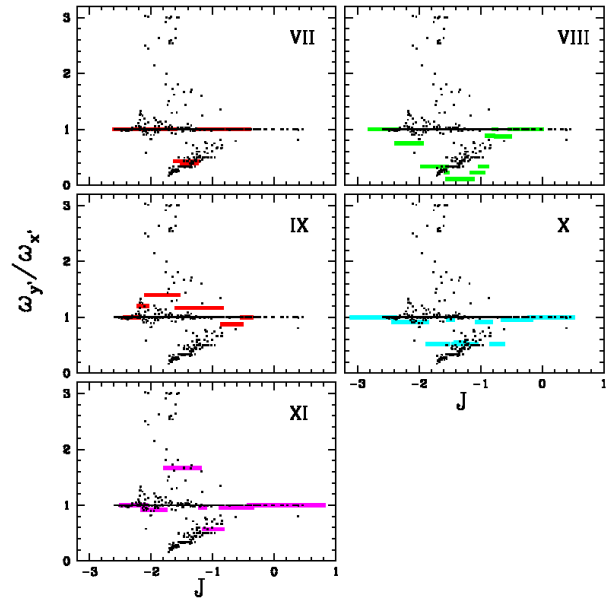


**Figure 39.** As in Figure 38, here for families VII to XI.

Galactic plane, will have a tube orbital projection on this plane which resembles the corresponding periodic orbit in the family. Only if this tube orbit is sufficiently narrow, the dominant frequencies in the  $x'$  and  $y'$  directions will be similar in both the projected and periodic orbits. The examples given in Figures 29, 30, and 31 show that some resulting tube orbital projections of three-dimensional orbits in regions D,E,F may have an appreciable thickness; thus, their dominant frequencies may differ from those obtained in the resonant family. This is shown explicitly in the next three figures 43, 44, and 45 commented below. The conclusion from

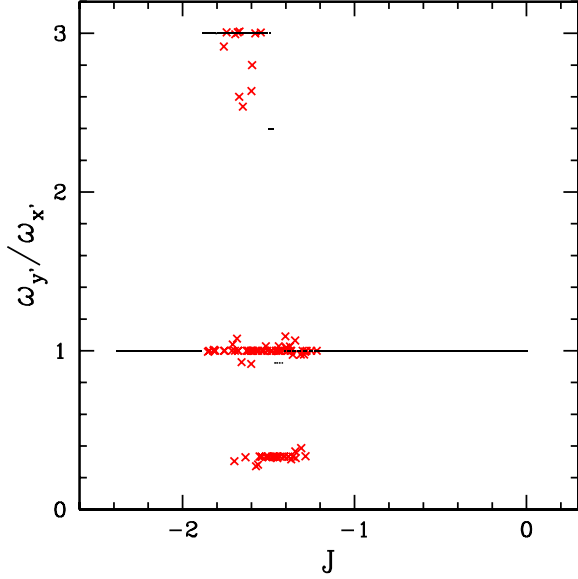


**Figure 40.** Comparison in a diagram  $\omega_{y'}/\omega_{x'}$  versus  $J$  between the family V of periodic orbits (black lines) and the region D in Figure 21 (red points).

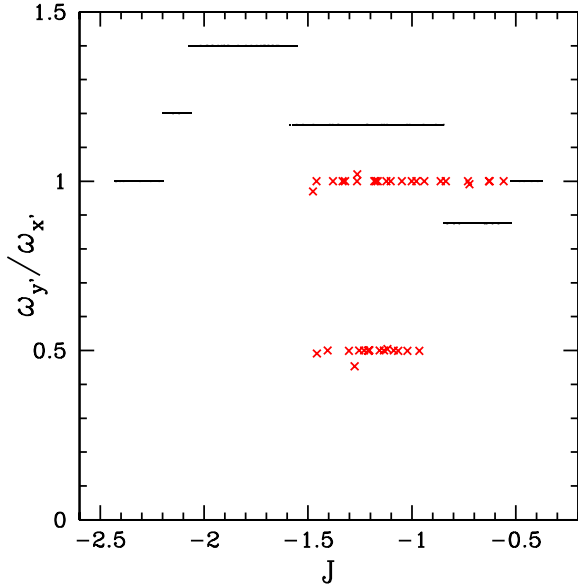


**Figure 41.** Same as in Figure 40, here for the family IX of periodic orbits and the region E in Figure 21.

this analysis of frequencies is that a diagram  $\omega_{y'}/\omega_{x'}$  versus  $J$  may not give a complete answer concerning the trapping of a three-dimensional orbit by a resonant family on the Galactic plane; it is necessary to complement the analysis with figures showing the orbital projection on this plane, and include other frequencies in the spectrum, as commented in the following. As concluded in the previous section, and complemented with the analysis in this section, the halo regions D,E,F have stars that are trapped by resonant families on the Galactic plane.

An alternate form to present the results in Figures 40,

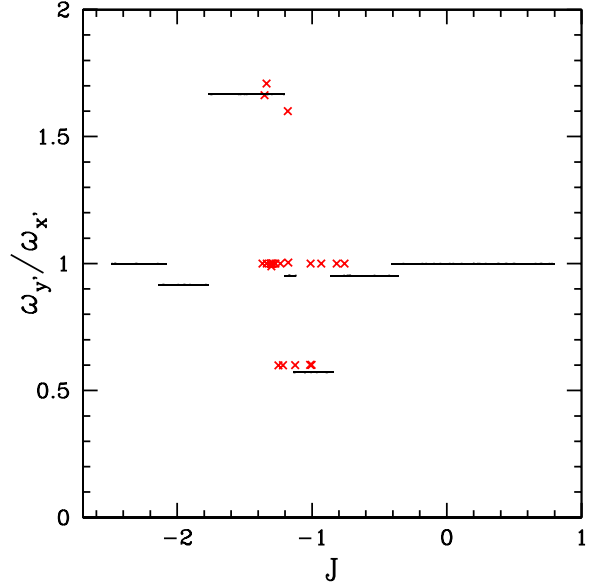


**Figure 42.** Same as in Figure 40, here for the family XI of periodic orbits and the region F in Figure 21.

41, and 42 is to plot directly the dominant frequencies  $f_{x'}$ ,  $f_{y'}$  in the  $x'$  and  $y'$  coordinates versus  $J$ . This is shown in Figures 43, 44, and 45. The frequencies are given in  $(\text{unit of time})^{-1} = (\text{UT})^{-1}$ , with  $1 \text{ UT} = 0.1 \text{ kpc km}^{-1} \text{ sec} = 9.784 \times 10^7 \text{ yr}$ . In these figures the red and blue lines show respectively the values of  $f_{x'}$  and  $f_{y'}$  for the given family of periodic orbits. The points (i.e. crosses) with magenta and cyan colours show the corresponding values of  $f_{x'}, f_{y'}$  for stars in the given region. As commented above, and explicitly shown in these figures,  $f_{x'}, f_{y'}$  for a three-dimensional orbit in a given region may not coincide with those obtained in the associated resonant family. A more complete comparison would be obtained with these type of figures by plotting not only the dominant frequencies in each case, but also other peak frequencies in the corresponding spectrum, especially if there are peaks with power similar to that obtained in the dominant frequency and thus not considered in the previous figures.

## 8 APPLICATION OF THE METHOD

To illustrate the possible relation between the agglomerations of stars trapped by resonances obtained in the empirical diagram of characteristic energy versus  $J$  presented in Section 4 and groups of stars catalogued as moving groups, the position of the Kapteyn group, a known moving group in the Galactic halo, is considered for this diagram. The 1642 halo stars and disc stars in the solar neighbourhood presented in Section 2 are again employed to delineate this diagram; they serve as a reference to compare with the corresponding positions in the diagram of the sample stars in the Kapteyn group. In fact, some of these 1642 stars are members of this moving group.

Eighteen member stars of the Kapteyn moving group have been selected from Eggen (1965a, 1977, 1990, 1996a,b) and Wylie-de Boer et al. (2010). The positions, proper mo-

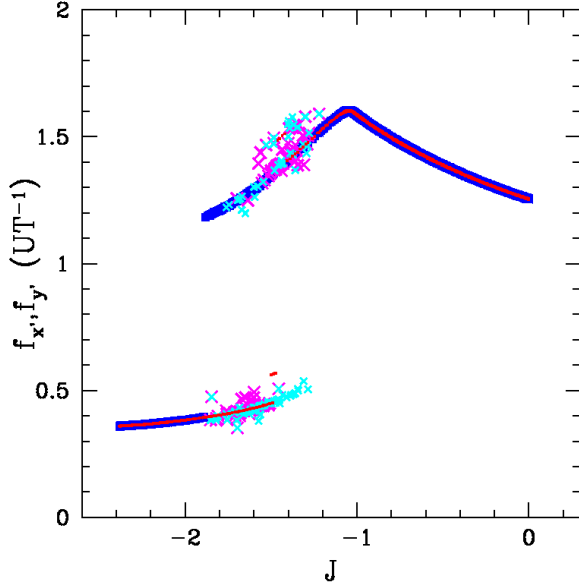


**Figure 43.** The frequencies  $f_{x'}$ ,  $f_{y'}$  in  $(\text{UT})^{-1}$ , with  $1 \text{ UT} = 0.1 \text{ kpc km}^{-1} \text{ sec}$ , for the family V of periodic orbits and the region D in Figure 21. The red and blue lines show respectively the values of  $f_{x'}$ ,  $f_{y'}$  for the family V and the points with magenta and cyan colours show respectively the values of  $f_{x'}$ ,  $f_{y'}$  for the region D.

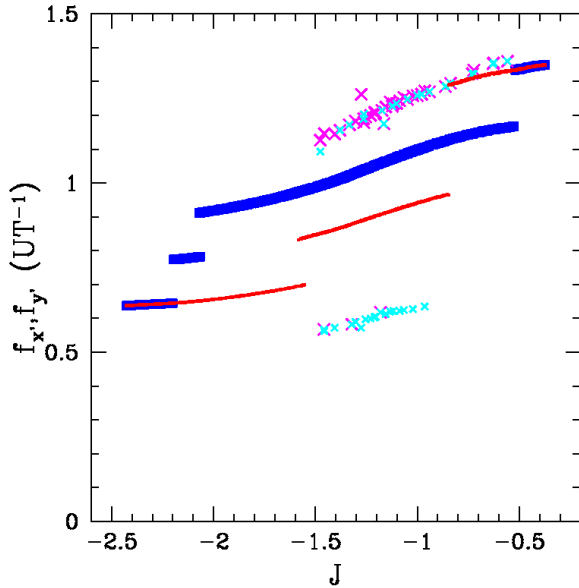


**Figure 44.** As in Figure 43, here for the family IX and the region E.

tions, radial velocities, and distances of these stars have been improved as was performed for the sample of 1642 stars.

Figure 46 shows the diagram with the observational points employed in Section 4 and some curves of families of periodic orbits of Section 5, along with red points corresponding to stellar members of the Kapteyn moving group. Comparing with Figure 6, these members arrange mainly around families III, IV, and V. However, only the family V has a stable part in its corresponding region covered by these

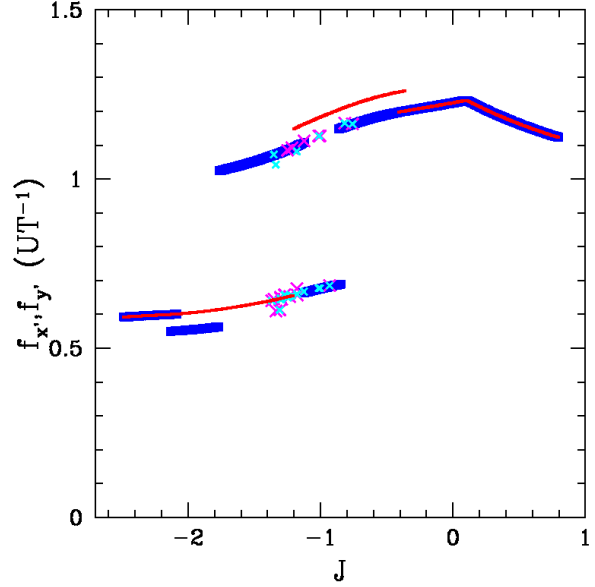


**Figure 45.** As in Figure 43, here for the family XI and the region F.

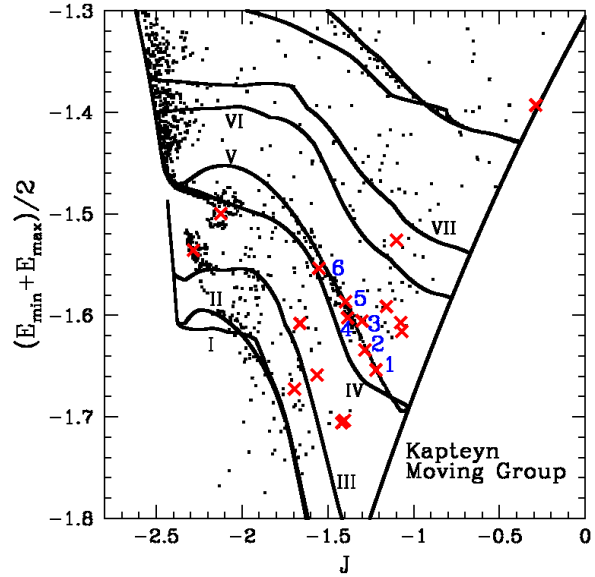


**Figure 46.** Diagram of characteristic energy versus  $J$  in the non-axisymmetric Galactic potential with the bar, showing with red points the positions of 18 members of the Kapteyn moving group. The small black dots correspond to the sample stars employed in Section 4; the black curves are some families of periodic orbits given in Section 5. The orbits of points (stars) marked as 1 to 6 are presented in Figures 47, and 48.

member stars; thus, the points marked as 1 to 6 in Figure 46 might have at the present time a relation with this resonant family V.

To see if this relation exists, for the six points (stars) marked as 1 to 6 in Figure 46, members of the Kapteyn moving group, Figures 47 and 48 show at the left side their corresponding orbital projections on the Galactic plane, plotted in the  $x', y'$  frame where the bar is at rest. Their meridional

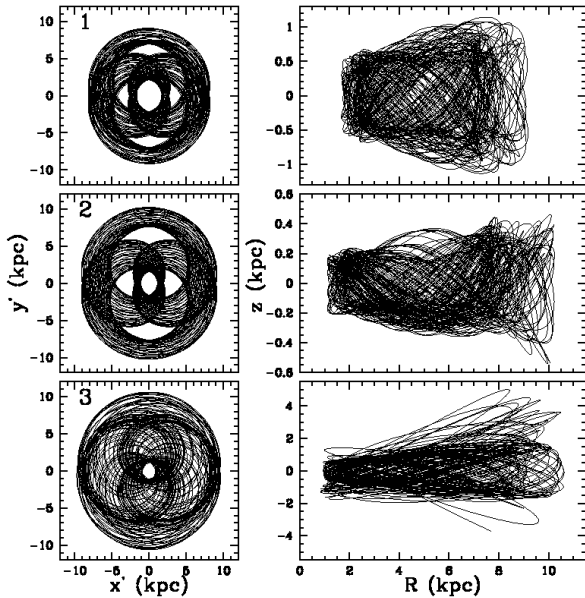


**Figure 47.** For the three points marked as 1,2,3 in Figure 46, the frames on the left show the corresponding orbital projections on the Galactic plane in the  $x', y'$  axes, and the frames on the right show the meridional orbits.

orbits are shown on the right side. Points 1,2,4 have an orbital projection on the Galactic plane which is a tube orbit, of the type that would be obtained around stable periodic orbits in the family V (see panel 2 of Figure 14), in accordance with their positions on this family, as shown in Figure 46. On the other hand, points 3 and 6 are very close to the curve of the family V, but their orbital projections on the Galactic plane resemble an orbit departing from the unstable periodic orbits in the family IV (see frame 3 in Figure 13). The orbit corresponding to point 5 does not seem to be associated with any resonance. Thus, the majority of the member stars of the Kapteyn moving group does not appear to have a relation with a resonant family on the Galactic plane.

On the other hand, a direct connection between the Kapteyn moving group and the well studied globular cluster  $\omega$  Centauri has been argued by Wylie-de Boer et al. (2010) using detailed kinematical and chemical analyses. They propose that many, or all, members of this moving group have been left behind as remnants as this globular cluster (ex-dwarf galaxy) was dragged into the Galaxy by dynamical friction. Meza et al. (2005) have carried out numerical simulations of such a process, and find a local group of stars which seem to relate to  $\omega$  Cen both in their angular momenta and in their chemical abundance characteristics. Silva et al. (2012) use the Bottlinger, Toomre and  $[\text{Fe}/\text{H}], V(\text{rot})$  diagrams to identify in the solar neighbourhood halo moving-group candidates relating to both the Kapteyn and the  $\omega$  Cen entities. Schuster et al. (2012) conclude that  $\omega$  Cen may have contributed in a significant way to their ‘low-alpha’ local halo component. If the Kapteyn group is of ‘cosmological’ origin, i.e. all stars having formed together in  $\omega$  Cen, then the appearance of Figure 46 may be due to the migration of the Kapteyn stars to the nearby resonant families III, IV, and V during their trajectories while being

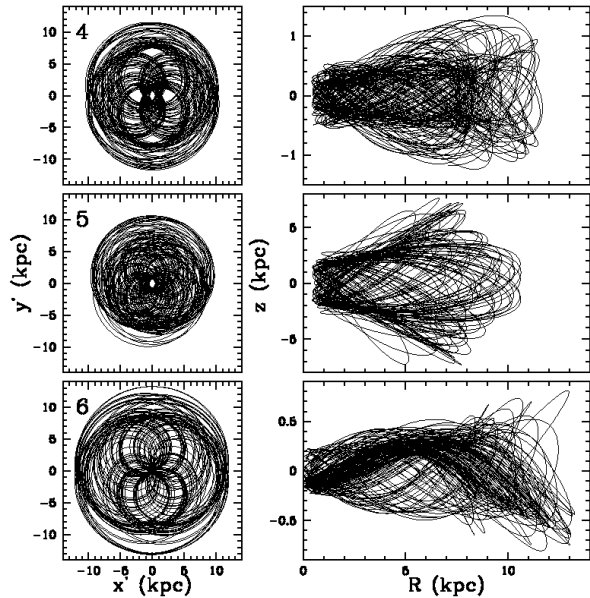


**Figure 48.** As in Figure 47, here for the three points marked as 4,5,6 in Figure 46.

lost to the Galaxy from  $\omega$  Cen. That is, Figure 46 seems to suggest a possible secular origin for the Kapteyn moving group, i.e. a product of the resonant trapping by the Galactic bar, but this is misleading, as shown here.

In a second paper, other moving groups in the Galactic halo will be analysed using the diagram of characteristic energy versus  $J$ . The method will also be applied to some known moving groups in the the Galactic disc.

## 9 CONCLUSIONS

In this study we have analysed the trapping of stars by resonances on the Galactic plane created by the Galactic bar. Our aim is to relate this mechanism with moving groups in our Galaxy, especially with moving groups in the Galactic halo. A new method is presented to delineate the trapping regions. To show how the method works, a sample of halo stars and disc stars in the solar neighbourhood has been employed. The orbits of these sample stars are computed in a nonaxisymmetric Galactic potential, and empirical diagrams are constructed using some particular orbital properties. These diagrams plot a characteristic energy versus a characteristic angular momentum, or a characteristic energy versus the orbital Jacobi constant, if the Galactic potential employs only the bar as its nonaxisymmetric component.

Some agglomerations of points in the disc and halo regions are obtained in these diagrams, which coincide with some families of periodic orbits on the Galactic plane, induced by the Galactic bar and plotted in the same diagrams. The influence of these resonant families can extend some kpc from the Galactic plane, explaining the observed coincidence in the halo region. Our future aim with this analysis is to investigate if these agglomerations obtained in the disc and halo can be the sites where some known moving groups lie.

The proposed method has been illustrated here with the Kapteyn group, a known moving group in the Galactic halo,



resulting in that a majority of member stars in this group does not have a relation with any of the resonant families or periodic orbits obtained in the employed Galactic potential, instead, we propose that these group might rather have an origin on the dissolution of a dwarf galaxy or a globular cluster. In a second paper the method will be applied to other groups in the Galactic halo, including also some known moving groups in the disc, to provide one piece of information on their possible, or not, resonant origin.

## ACKNOWLEDGEMENTS

We thank the anonymous referee for a very careful review and several excellent suggestions that greatly improved this work. Based upon observations acquired at the Observatorio Astronómico Nacional in the Sierra San Pedro Mártir (OAN-SPM), Baja California, México. We thank Agustín Márquez, Benjamín Hernández, Sergio Silva, and Maru Contreras for their contributions, and also the technical staff at SPM, especially Gabriel García (deceased), Gustavo Melgoza, and Felipe Montalvo. The authors acknowledge financial support from UNAM-DGAPA PAPIIT IN114114 and IN103014 grants, and the CONACyT (México) projects 27884-E, CB-2005-49434, and CB-2005-49002. We also acknowledge the use of the SIMBAD data base at the CDS, Strasbourg, France, and the ADS of the SAO/NASA.

## REFERENCES

- Abt H. A., Biggs E. S., 1972, *Bibliography of Stellar Radial Velocities*, Microfiche version. Centre de Données Stellaires, Observatoire de Strasbourg
- Allen C., Santillán A., 1991, *Rev. Mex. Astron. Astrofis.*, 22, 255
- Antoja T., Valenzuela O., Pichardo B., Moreno E., Figueras F., Fernández D., 2009, *ApJL*, 700, L78
- Antoja T., Figueras F., Romero-Gómez M., Pichardo B., Valenzuela O., Moreno E., 2011, *MNRAS*, 418, 1423
- Antoja T. et al., 2014, *A&A*, 563, A60
- Athanassoula E., 2002, *ApJL*, 569, L83
- Babusiaux C., Gilmore, G., 2005, *MNRAS*, 358, 1309
- Barbier-Brossat M., Figon P., 2000, *A&AS*, 142, 217
- Barbier-Brossat M., Petit M., Figon P., 1994, *A&AS*, 108, 603
- Benjamin R. A. et al., 2005, *ApJL*, 630, L149
- Binney J., Gerhard O. E., Stark A. A., Bally J., Uchida K. I., 1991, *MNRAS*, 252, 210
- Binney J., Tremaine S. 2008, *Galactic Dynamics* 2nd Ed. (Princeton: Princeton University Press)
- Bissantz N., Gerhard O., 2002, *MNRAS*, 330, 591
- Blum R. D., 1995, *ApJL*, 444, L89
- Bottlinger K. F., 1932, *Ergebn. d.Exacten. Naturwiss.*, 11, 31
- Brunthaler A. et al., 2011, *AN*, 332, No. 5, 461
- Buta R., Vasylyev S., Salo H., Laurikainen E., 2005, *AJ*, 130, 506
- Carney B. W., Latham D. W., Laird J. B., Aguilar L. A., 1994, *AJ*, 107, 2240
- Ceverino D., Klypin A., 2007, *MNRAS*, 379, 1155
- Churchwell E. et al., 2009, *PASP*, 121, 213
- Combes F., Sanders R. H., 1981, *A&A*, 96, 164
- de Bruijne J. H. J., 1999, *MNRAS*, 306, 381
- Dehnen W., 2000, *AJ*, 119, 800
- Drimmel R., 2000, *A&A*, 358, L13
- Dwek E. et al., 1995, *ApJ*, 445, 716
- Eggen O. J., 1958, *MNRAS*, 118, 154
- Eggen O. J., 1959, *Obs*, 79, 88
- Eggen O. J., 1960a, *MNRAS*, 120, 430
- Eggen O. J., 1960b, *MNRAS*, 120, 563
- Eggen O. J., 1965a, in *Galactic Structure*, Vol. 5, Stars and Stellar Systems, Univ. of Chicago Press, p. 127
- Eggen O. J., 1965b, *Obs*, 85, 191
- Eggen O. J., 1970, *PASP*, 82, 99
- Eggen O. J., 1971a, *PASP*, 83, 251
- Eggen O. J., 1971b, *PASP*, 83, 271
- Eggen O. J., 1974, *PASP*, 86, 162
- Eggen O. J., 1976, *PASP*, 88, 426
- Eggen O. J., 1977, *ApJ*, 215, 812
- Eggen O. J., 1983, *AJ*, 88, 813
- Eggen O. J., 1990, *AJ*, 100, 1159
- Eggen O. J., 1996a, *AJ*, 112, 1595
- Eggen O. J., 1996b, *AJ*, 112, 2661
- Eggen O. J., Sandage A. R., 1959, *MNRAS*, 119, 255
- ESA 1997, *The Hipparcos and Tycho Catalogues*, ESA SP-1200 (Noordwijk, Netherlands: ESA Publications Division)
- Fouts G., Sandage A., 1986, *AJ*, 91, 1189
- Freudenreich H. T., 1998, *ApJ*, 492, 495
- Fux R., 2001, *A&A*, 373, 511
- Gerhard O., 2002, in Da Costa G. S., Jerjen H., eds, *ASP Conf. Ser. 273, The Dynamics, Structure & History of Galaxies: A Workshop in Honour of Professor Ken Freeman*. Astron. Soc. Pac. (San Francisco, CA: ASP), p. 73
- Gerhard O., 2011, *MSAIS*, Vol. 18, 185
- Giclas H. L., Slaughter C. D., Burnham R. Jr., 1959, *Lowell Obs. Bull.*, 4, 136
- Giclas H. L., Burnham R. Jr., Thomas N. G., 1961, *Lowell Obs. Bull.*, 5, 61
- Giclas H. L., Burnham R. Jr., Thomas N. G., 1975, *Lowell Obs. Bull.*, 8, 9
- Helmi A., de Zeeuw P. T., 2000, *MNRAS*, 319, 657
- Hénon M., 1965, *AnAp*, 28, 992
- Høg E. et al., 2000, *A&A*, 355, L27 (the Tycho-2 Catalogue)
- Hoogerwerf R., Aguilar L. A., 1999, *MNRAS*, 306, 394
- Johnston K. V., Hernquist L., Bolte M., 1996, *ApJ*, 465, 278
- Kent S. M., 1992, *ApJ*, 387, 181
- Luyten W. J., 1979a, *NLTT Catalogue* (Minneapolis: University of Minnesota)
- Luyten W. J., 1979b, *LHS Catalogue* (Minneapolis: University of Minnesota)
- Lynden-Bell D., 1999, in Gibson B. K., Axelrod T. S., Putman M. E., eds, *ASP Conf. Ser. 165, The Third Stromlo Symposium: The Galactic Halo*. Astron. Soc. Pac., San Francisco, p. 17
- Lynden-Bell D., Kalnajs A. J., 1972, *MNRAS*, 157, 1
- Lynden-Bell D., Lynden-Bell R. M., 1995, *MNRAS*, 275, 429
- Majewski S. R., 1994, *ApJL*, 431, L17
- Majewski S. R., Hawley S. L., Munn J. A., 1996, in Morrison H., Sarajedini A., eds, *ASP Conf. Ser. 92, Formation*

- of the Galactic Halo...Inside and Out. Astron. Soc. Pac., San Francisco, p. 119
- Martinez-Valpuesta I., Shlosman I., Heller C., 2006, *ApJ*, 637, 214
- Meza A., Navarro J. F., Abadi M. G., Steinmetz M., 2005, *MNRAS*, 359, 93
- Minchev I., Nordhaus J., Quillen A. C., 2007, *ApJL*, 664, L31
- Peñarrubia J., Walker M. G., Gilmore G., 2009, *MNRAS*, 399, 1275
- Pichardo B., Martos M., Moreno E., Espresate J., 2003, *ApJ*, 582, 230
- Pichardo B., Martos M., Moreno E., 2004, *ApJ*, 609, 144
- Pichardo B., Moreno E., Allen C., Bedin L. R., Bellini A., Pasquini L., 2012, *AJ*, 143, 73
- Press W. H., Teukolsky S. A., Vetterling W. T., Flannery B. P., 1992, *Numerical Recipes in Fortran 77: The Art of Scientific Computing* (2nd ed.; Cambridge: Cambridge Univ. Press)
- Proctor R. A., 1869, *Proc. R. Soc. London*, 18, 169
- Quillen A. C., Dougherty J., Bagley M. B., Minchev I., Comparetta J., 2011, *MNRAS*, 417, 762
- Rojas-Niño A., Valenzuela O., Pichardo B., Aguilar L. A., 2012, *ApJL*, 757, L28
- Rojas-Niño A., Martínez-Medina L., Pichardo B., Valenzuela O., 2015, *ApJ*, submitted
- Roman N. G., 1949, *ApJ*, 110, 205
- Röser S., Bastian U., 1991, *PPM Star Catalogue by the Astronomisches Rechen-Institut Heidelberg* (Heidelberg: Spektrum Akademischer Verlag)
- Ryan S. G., Norris J. E., 1991, *AJ*, 101, 1835
- Salim S., Gould A., 2003, *ApJ*, 582, 1011
- Sanders R. H., Tubbs A. D., 1980, *ApJ*, 235, 803
- Schuster W. J., Nissen P. E., 1988, *A&AS*, 73, 225
- Schuster W. J., Parrao L., Contreras M. E., 1993, *A&AS*, 97, 951
- Schuster W. J., Allen C., 1997, *A&A*, 319, 796
- Schuster W. J., Beers T. C., Michel R., Nissen P. E., García G., 2004, *A&A*, 422, 527
- Schuster W. J., Moitinho A., Márquez A., Parrao L., Covarrubias E., 2006, *A&A*, 445, 939
- Schuster W. J., Moreno E., Nissen P. E., Pichardo B., 2012, *A&A*, 538, A21
- Sellwood J. A., 2014, *Rev. Mod. Phys.*, 86, 1
- Silva J. S., Schuster W. J., Contreras M. E., 2012, *Rev. Mex. Astron. Astrofis.*, 48, 109
- Soderblom D. R., Mayor M., 1993, *AJ*, 105, 226
- Stanek K. Z., Udalski A., Szymański M., KaLuZny J., Kuźbiak Z. M., Mateo M., Krzemiński W., 1997, *ApJ*, 477, 163
- Tremaine S., Weinberg M. D., 1984, *MNRAS*, 209, 729
- Trumpler R. J., Weaver H. F., 1953, *‘Statistical Astronomy’*, (Berkeley and Los Angeles: University of California Press), pp.588-592
- Weinberg M. D., Katz N., 2007a, *MNRAS*, 375, 425
- Weinberg M. D., Katz N., 2007b, *MNRAS*, 375, 460
- Weiner B. J., Sellwood J. A., 1999, *ApJ*, 524, 112
- Wilson R. E., Raymond H., 1938, *AJ*, 47, 49
- Wylie-de Boer E., Freeman K., Williams M., 2010, *AJ*, 139, 636
- Zhao H., 1994, PhD thesis, Columbia Univ.